



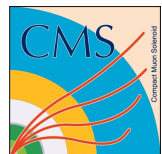
Universiteit Gent
Faculteit Wetenschappen
Vakgroep Fysica en Sterrenkunde

² No title yet

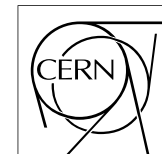
³ No sub-title neither, obviously...

⁴ Alexis Fagot

⁵



Thesis to obtain the degree of
Doctor of Philosophy in Physics
Academic years 2012-2017



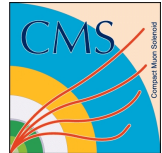


Universiteit Gent
Faculteit Wetenschappen
Vakgroep Fysica en Sterrenkunde

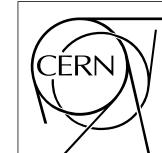
Promotoren: Dr. Michael Tytgat
Prof. Dr. Dirk Ryckbosch

Universiteit Gent
Faculteit Wetenschappen
Vakgroep Fysica en Sterrenkunde
Proeftuinstraat 86, B-9000 Gent, België
Tel.: +32 9 264.65.28
Fax.: +32 9 264.66.97

17



Thesis to obtain the degree of
Doctor of Philosophy in Physics
Academic years 2012-2017



Acknowledgements

¹⁹ Ici on remerciera tous les gens que j'ai pu croiser durant cette aventure et qui m'ont
²⁰ permis de passer un bon moment

²¹ *Gent, ici la super date de la mort qui tue de la fin d'écriture*
²² *Alexis Fagot*

Table of Contents

23

24	Acknowledgements	i
25	Nederlandse samenvatting	xvii
26	English summary	xix
27	1 Introduction	1-1
28	1.1 A story of High Energy Physics	1-1
29	1.2 Organisation of this study	1-1
30	2 Investigating the TeV scale	2-1
31	2.1 The Standard Model of Particle Physics	2-1
32	2.2 The Large Hadron Collider and the Compact Muon Solenoid	2-1
33	2.3 Muon Phase-II Upgrade	2-1
34	3 Amplification processes in gaseous detectors	3-1
35	3.1 Signal formation	3-1
36	3.2 Gas transport parameters	3-1
37	4 Resistive Plate Chambers	4-1
38	4.1 Principle	4-1
39	4.2 Rate capability of Resistive Plate Chambers	4-1
40	4.3 High time resolution	4-1
41	4.4 Resistive Plate Chambers at CMS	4-1
42	4.4.1 Overview	4-1
43	4.4.2 The present RPC system	4-2
44	4.4.3 Pulse processing of CMS RPCs	4-3
45	5 Longevity studies and Consolidation of the present CMS RPC subsystem	5-1
46	5.1 Testing detectors under extreme conditions	5-1
47	5.1.1 The Gamma Irradiation Facilities	5-3
48	5.1.1.1 GIF	5-3
49	5.1.1.2 GIF++	5-5
50	5.2 Preliminary tests at GIF	5-8
51	5.2.1 Resistive Plate Chamber test setup	5-8

53	5.2.2	Data Acquisition	5-10
54	5.2.3	Geometrical acceptance of the setup layout to cosmic muons	5-10
55	5.2.3.1	Description of the simulation layout	5-11
56	5.2.3.2	Simulation procedure	5-13
57	5.2.3.3	Results	5-14
58	5.2.4	Photon flux at GIF	5-15
59	5.2.4.1	Expectations from simulations	5-15
60	5.2.4.2	Dose measurements	5-19
61	5.2.5	Results and discussions	5-20
62	5.3	Longevity tests at GIF++	5-21
63	5.3.1	Description of the Data Acquisition	5-25
64	5.3.2	RPC current, environmental and operation parameter monitoring	5-26
65	5.3.3	Measurement procedure	5-27
66	5.3.4	Longevity studies results	5-27
68	6	Investigation on high rate RPCs	6-1
69	6.1	Rate limitations and ageing of RPCs	6-1
70	6.1.1	Low resistivity electrodes	6-1
71	6.1.2	Low noise front-end electronics	6-1
72	6.2	Construction of prototypes	6-1
73	6.3	Results and discussions	6-1
74	7	Conclusions and outlooks	7-1
75	7.1	Conclusions	7-1
76	7.2	Outlooks	7-1
77	A	A data acquisition software for CAEN VME TDCs	A-1
78	A.1	GIF++ DAQ file tree	A-1
79	A.2	Description of the readout setup	A-2
80	A.3	Data read-out	A-5
81	A.3.1	V1190A TDCs	A-5
82	A.3.2	DataReader	A-8
83	A.3.3	V1718 USB Bridge	A-12
84	A.3.4	Configuration file	A-13
85	A.3.5	DAQ algorithm overview	A-16
86	A.4	Software export	A-16
87	B	Details on the online analysis package	B-1
88	B.1	Introduction	B-1
89	C	Structure of the hybrid simulation software	C-1
90	C.1	Introduction	C-1

List of Figures

91

92	2.1	Absorbed dose in the CMS cavern after an integrated luminosity of 3000 fb. R is the transverse distance from the beamline and Z is the distance along the beamline from the Interaction Point at Z=0.	2-2
93			
94			
95	2.2	A quadrant of the muon system, showing DTs (yellow), RPCs (light blue), and CSCs (green). The locations of new forward muon detectors for Phase-II are contained within the dashed box and indicated in red for GEM stations (ME0, GE1/1, and GE2/1) and dark blue for improved RPC (iRPC) stations (RE3/1 and RE4/1).	2-3
96			
97			
98			
99			
100	2.3	RMS of the multiple scattering displacement as a function of muon p_T for the proposed forward muon stations. All of the electromag- netic processes such as bremsstrahlung and magnetic field effect are included in the simulation.	2-4
101			
102			
103			
104	4.1	Signals from the RPC strips are shaped by the FEE described on Figure 4.1a. Output LVDS signals are then read-out by a TDC module connected to a computer or converted into NIM and sent to scalers. Figure 4.1b describes how these converted signals are put in coincidence with the trigger.	4-4
105			
106			
107			
108			
109	4.2	Description of the principle of a CFD. A comparison of threshold triggering (left) and constant fraction triggering (right) is shown in Figure 4.2a. Constant fraction triggering is obtained thanks to zero-crossing technique as explained in Figure 4.2b. The signal arriving at the input of the CFD is split into three components. A first one is delayed and connected to the inverting input of a first comparator. A second component is connected to the noninverting input of this first comparator. A third component is connected to the noninverting input of another comparator along with a thresh- old value connected to the inverting input. Finally, the output of both comparators is fed through an AND gate.	4-5
110			
111			
112			
113			
114			
115			
116			
117			
118			
119			
120	5.1	(5.1a) Extrapolation from 2016 data of single hit rate per unit area in the barrel region. (5.1b) Extrapolation from 2016 data of single hit rate per unit area in the endcap region.	5-2
121			
122			

123	5.2	Background Fluka simulation compared to 2016 Data at $L = 10^{34} \text{ cm}^{-2} \cdot \text{s}^{-1}$ in the fourth endcap disk region. A mismatch in between simulation and data can be observed. [To be understood.]	5-3
126	5.3	Layout of the test beam zone called X5c GIF at CERN. Photons from the radioactive source produce a sustained high rate of random hits over the whole area. The zone is surrounded by 8 m high and 80 cm thick concrete walls. Access is possible through three entry points. Two access doors for personnel and one large gate for material. A crane allows installation of heavy equipment in the area.	5-4
133	5.4	^{137}Cs decays by β^- emission to the ground state of ^{137}Ba (BR = 5.64%) and via the 662 keV isomeric level of ^{137}Ba (BR = 94.36%) whose half-life is 2.55 min.	5-5
136	5.5	Floor plan of the GIF++ facility. When the facility downstream of the GIF++ takes electron beam, a beam pipe is installed along the beam line (z-axis). The irradiator can be displaced laterally (its center moves from $x = 0.65$ m to 2.15 m), to increase the distance to the beam pipe.	5-6
141	5.6	Simulated unattenuated current of photons in the xz plane (Figure 5.6a) and yz plane (Figure 5.6b) through the source at $x = 0.65$ m and $y = 0$ m. With angular correction filters, the current of 662 keV photons is made uniform in xy planes.	5-7
145	5.7	Description of the RPC setup. Dimensions are given in mm. A tent containing RPCs is placed at 1720 mm from the source container. The source is situated in the center of the container. RE-4-2-BARC-161 chamber is 160 mm inside the tent. This way, the distance between the source and the chambers plan is 2060 mm. Figure 5.7a provides a side view of the setup in the xz plane while Figure 5.7b shows a top view in the yz plane.	5-8
152	5.8	RE-4-2-BARC-161 chamber is inside the tent as described in Figure 5.7. In the top right, the two scintillators used as trigger can be seen. This trigger system has an inclination of 10° relative to horizontal and is placed above half-partition B2 of the RPCs. PMT electronics are shielded thanks to lead blocks placed in order to protect them without stopping photons from going through the scintillators and the chamber.	5-9

159	5.9 Hit distributions over all 3 partitions of RE-4-2-BARC-161 chamber is showed on these plots. Top, middle and bottom figures respectively correspond to partitions A, B, and C. These plots show that some events still occur in other half-partitions than B2, which corresponds to strips 49 to 64, in front of which the trigger is placed, contributing to the inefficiency of detection of cosmic muons.	5-10
160		
161		
162		
163		
164		
165		
166		
167		
168		
169	5.10 Results are derived from data taken on half-partition B2 only. On the 18 th of June 2014, data has been taken on chamber RE-2-BARC-161 at building 904 (Prevessin Site) with cosmic muons providing us a reference efficiency plateau of $(97.54 \pm 0.15)\%$ represented by a black curve. A similar measurement has been done at GIF on the 21 st of July with the same chamber giving a plateau of $(78.52 \pm 0.94)\%$ represented by a red curve.	5-11
170		
171		
172		
173		
174		
175		
176	5.11 Representation of the layout used for the simulations of the test setup. The RPC is represented as a yellow trapezoid while the two scintillators as blue cuboids looking at the sky. A green plane corresponds to the muon generation plane within the simulation. Figure 5.7a shows a global view of the simulated setup. Figure 5.7b shows a zommed view that allows to see the 2 scintillators as well as the full RPC plane.	5-12
177		
178		
179		
180		
181		
182		
183	5.12 γ flux $F(D)$ is plot using values from table 5.1. As expected, the plot shows similar attenuation behaviours with increasing distance for each absorption factors.	5-15
184		
185		
186	5.13 Figure 5.13a shows the linear approximation fit done via formulae 5.7 on data from table 5.2. Figure 5.13b shows a comparison of this model with the simulated flux using a and b given in figure 5.13a in formulae 5.4 and the reference value $D_0 = 50\text{cm}$ and the associated flux for each absorption factor F_0^{ABS} from table 5.1	5-17
187		
188		
189		
190		
191		
192	5.14 Dose measurements has been done in a plane corresponding to the tents front side. This plan is 1900 mm away from the source. As explained in the first chapter, a lens-shaped lead filter provides a uniform photon flux in the vertical plan orthogonal to the beam direction. If the second line of measured fluxes is not taken into account because of lower values due to experimental equipments in the way between the source and the tent, the uniformity of the flux is well showed by the results.	5-19
193		
194		
195		
196		
197		
198		
199		
200	5.15	5-20

201	5.16 Evolution of the maximum efficiency for RE2 (5.16a) and RE4 202 (5.16b) chambers with increasing extrapolated γ rate per unit area 203 at working point. Both irradiated (blue) and non irradiated (red) 204 chambers are shown.	5-22
205	5.17 Evolution of the working point for RE2 (5.17a) and RE4 (5.17b) 206 with increasing extrapolated γ rate per unit area at working point. 207 Both irradiated (blue) and non irradiated (red) chambers are shown. 5-23	
208	5.18 Evolution of the maximum efficiency at HL-LHC conditions, i.e. 209 a background hit rate per unit area of 300 Hz/cm ² , with increasing 210 integrated charge for RE2 (5.18a) and RE4 (5.18b) detectors. Both 211 irradiated (blue) and non irradiated (red) chambers are shown. The 212 integrated charge for non irradiated detectors is recorded during 213 test beam periods and stays small with respect to the charge accu- 214 mulated in irradiated chambers.	5-23
215	5.19 Comparison of the efficiency sigmoid before (triangles) and after 216 (circles) irradiation for RE2 (5.19a) and RE4 (5.19b) detectors. 217 Both irradiated (blue) and non irradiated (red) chambers are shown. 5-24	
218	5.20 Evolution of the Bakelite resistivity for RE2 (5.20a) and RE4 (5.20b) 219 detectors. Both irradiated (blue) and non irradiated (red) chambers 220 are shown.	5-24
221	5.21 Evolution of the noise rate per unit area for the irradiated chamber 222 RE2-2-BARC-9 only.	5-25
223	A.1 (A.1a) View of the front panel of a V1190A TDC module [10]. 224 (A.1b) View of the front panel of a V1718 Bridge module [11]. 225 (A.1c) View of the front panel of a 6U 6021 VME crate [12]. . . . A-4	
226	A.2 Module V1190A <i>Trigger Matching Mode</i> timing diagram [10]. . . A-6	
227	A.3 Structure of the ROOT output file generated by the DAQ. The 5 228 branches (<code>EventNumber</code> , <code>number_of_hits</code> , <code>Quality_flag</code> , <code>TDC_channel</code> 229 and <code>TDC_TimeStamp</code>) are visible on the left panel of the ROOT 230 browser. On the right panel is visible the histogram corresponding 231 to the variable <code>nHits</code> . In this specific example, there were approxi- 232 mately 50k events recorded to measure the gamma irradiation rate 233 on the detectors. Each event is stored as a single entry in the <code>TTree</code> . A-12	
234	A.4 WebDCS DAQ scan page. On this page, shifters need to choose 235 the type of scan (Rate, Efficiency or Noise Reference scan), the 236 gamma source configuration at the moment of data taking, the 237 beam configuration, and the trigger mode. These information will 238 be stored in the DAQ ROOT output. Are also given the minimal 239 measurement time and waiting time after ramping up of the detec- 240 tors is over before starting the data acquisition. Then, the list of 241 HV points to scan and the number of triggers for each run of the 242 scan are given in the table underneath.	A-14

List of Tables

244	5.1	Total photon flux ($E\gamma \leq 662$ keV) with statistical error predicted considering a ^{137}Cs activity of 740 GBq at different values of the distance D to the source along the x-axis of irradiation field [6]. . .	5-15
245	5.2	Correction factor c is computed thanks to formulae 5.5 taking as reference $D_0 = 50$ cm and the associated flux F_0^{ABS} for each ab- sorption factor available in table 5.1.	5-16
246	5.3	The data at D_0 in 1997 is taken from [6]. In a second step, using Equations 5.8 and 5.9, the flux at D can be estimated in 1997. Then, taking into account the attenuation of the source activity, the flux at D can be estimated at the time of the tests in GIF in 2014. Finally, assuming a sensitivity of the RPC to γ $s = 2 \cdot 10^{-3}$, an estimation of the hit rate per unit area is obtained.	5-18
247			
248			
249			
250			
251			
252			
253			
254			
255			

256

List of Acronyms

257

List of Acronyms

258

259

A

261

262 AFL

Almost Full Level

263

264

B

266

267 BARC

Bhabha Atomic Research Centre

268 BLT

Block Transfer

269 BR

Branching Ratio

270

271

C

273

274 CAEN

Costruzioni Apparecchiature Elettroniche Nucleari S.p.A.

275

276 CERN

European Organization for Nuclear Research

277 CFD

Constant Fraction Discriminator

278 CMS

Compact Muon Solenoid

279 CSC

Cathode Strip Chamber

280

281

D

283

284 DAQ

Data Acquisition

285 DCS

Detector Control Software

286 DQM

Data Quality Monitoring

287	DT	Drift Tube
288		
289		
290	F	
291		
292	FEE	Front-End Electronics
293	FEB	Front-End Board
294		
295		
296	G	
297		
298	GE/-	Find a good description
299	GE1/1	Find a good description
300	GE2/1	Find a good description
301	GEANT	GEometry ANd Tracking - a series of software toolkit platforms developed by CERN
302		
303	GEM	Gas Electron Multiplier
304	GIF	Gamma Irradiation Facility
305	GIF++	new Gamma Irradiation Facility
306		
307		
308	H	
309		
310	HL-LHC	High Luminosity LHC
311	HV	High Voltage
312		
313		
314	I	
315		
316	iRPC	improved RPC
317	IRQ	Interrupt Request
318		
319		
320	L	
321		
322	LHC	Large Hadron Collider
323	LS1	First Long Shutdown
324	LS3	Third Long Shutdown

325	LV	Low Voltage
326	LVDS	Low-Voltage Differential Signaling
327		
328		
329	M	
330		
331	MC	Monte Carlo
332	MCNP	Monte Carlo N-Particle
333	ME-/-	Find good description
334	ME0	Find good description
335		
336		
337	N	
338		
339	NIM	Nuclear Instrumentation Module logic signals
340		
341		
342	P	
343		
344	PMT	PhotoMultiplier Tube
345		
346		
347	R	
348		
349	RE-/-	Find a good description
350	RE2/2	Find a good description
351	RE3/1	Find a good description
352	RE3/2	Find a good description
353	RE4/1	Find a good description
354	RE4/2	Find a good description
355	RE4/3	Find a good description
356	RMS	Root Mean Square
357	ROOT	a framework for data processing born at CERN
358	RPC	Resistive Plate Chamber
359		
360		
361	S	
362		
363	SPS	Super Proton Synchrotron

364

365

366 **T**

367

368 TDC

Time-to-Digital Converter

369

370

371 **W**

372

373 webDCS

Web Detector Control System

375

Nederlandse samenvatting –Summary in Dutch–

377 Le resume en Neerlandais (j'aurais peut-etre de apprendre la langue juste pour
378 ca...).

English summary

380 Le meme résume mais en Anglais (on commencera par la hein!).

1

Introduction

381

382

³⁸³ **1.1 A story of High Energy Physics**

³⁸⁴ **1.2 Organisation of this study**

2

385

386

Investigating the TeV scale

387 2.1 The Standard Model of Particle Physics

388 2.2 The Large Hadron Collider and the Compact 389 Muon Solenoid

390 2.3 Muon Phase-II Upgrade

391 After the more than two years lasting First Long Shutdown (LS1), the Large
392 Hadron Collider (LHC) delivered its very first Run-II proton-proton collisions
393 early 2015. LS1 gave the opportunity to the LHC and to its experiments to
394 undergo upgrades. The accelerator is now providing collisions at center-of-mass
395 energy of 13 TeV and bunch crossing rate of 40 MHz, with a peak luminosity ex-
396 ceeding its design value. During the first and upcoming second LHC Long Shut-
397 down, the Compact Muon Solenoid (CMS) detector is also undergoing a number
398 of upgrades to maintain a high system performance [1].

399 From the LHC Phase-II or High Luminosity LHC (HL-LHC) period onwards,
400 i.e. past the Third Long Shutdown (LS3), the performance degradation due to
401 integrated radiation as well as the average number of inelastic collisions per bunch
402 crossing, or pileup, will rise substantially and become a major challenge for the
403 LHC experiments, like CMS that are forced to address an upgrade program for
404 Phase-II [2]. Simulations of the expected distribution of absorbed dose in the CMS
405 detector under HL-LHC conditions, show in figure 5.14 that detectors placed close

406 to the beamline will have to withstand high irradiation, the radiation dose being of
407 the order of a few tens of Gy.

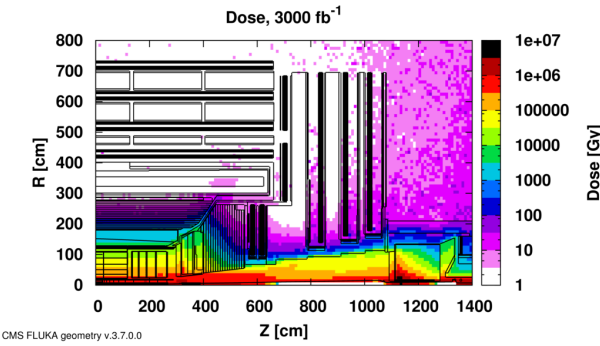


Figure 2.1: Absorbed dose in the CMS cavern after an integrated luminosity of 3000 fb. R is the transverse distance from the beamline and Z is the distance along the beamline from the Interaction Point at Z=0.

408 The measurement of small production cross-section and/or decay branching
409 ratio processes, such as the Higgs boson coupling to charge leptons or the $B_s \rightarrow$
410 $\mu^+ \mu^-$ decay, is of major interest and specific upgrades in the forward regions of
411 the detector will be required to maximize the physics acceptance on the largest
412 possible solid angle. To ensure proper trigger performance within the present cov-
413 erage, the muon system will be completed with new chambers. In figure 2.2 one
414 can see that the existing Cathode Strip Chambers (CSCs) will be completed by Gas
415 Electron Multipliers (GEMs) and Resistive Plate Chambers (RPCs) in the pseudo-
416 rapidity region $1.6 < |\eta| < 2.4$ to complete its redundancy as originally scheduled
417 in the CMS Technical Proposal [3].

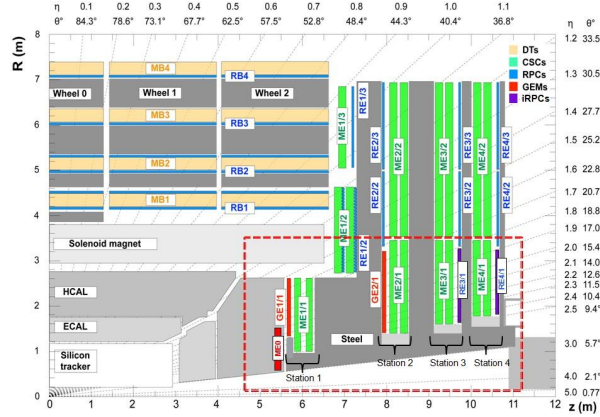


Figure 2.2: A quadrant of the muon system, showing DTs (yellow), RPCs (light blue), and CSCs (green). The locations of new forward muon detectors for Phase-II are contained within the dashed box and indicated in red for GEM stations (ME0, GE1/I, and GE2/I) and dark blue for improved RPC (iRPC) stations (RE3/I and RE4/I).

418 RPCs are used by the CMS first level trigger for their good timing performances.
 419 Indeed, a very good bunch crossing identification can be obtained with the
 420 present CMS RPC system, given their fast response of the order of 1 ns. In order
 421 to contribute to the precision of muon momentum measurements, muon chambers
 422 should have a spatial resolution less or comparable to the contribution of multiple
 423 scattering [1]. Most of the plausible physics is covered only considering muons
 424 with $p_T < 100$ GeV thus, in order to match CMS requirements, a spatial resolu-
 425 tion of $\mathcal{O}(\text{few mm})$ the proposed new RPC stations, as shown by the simulation in
 426 figure 2.3. According to preliminary designs, RE3/1 and RE4/1 readout pitch will
 427 be comprised between 3 and 6 mm and 5 η -partitions could be considered.

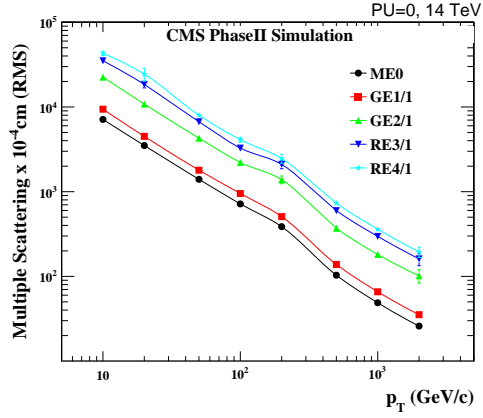


Figure 2.3: RMS of the multiple scattering displacement as a function of muon p_T for the proposed forward muon stations. All of the electromagnetic processes such as bremsstrahlung and magnetic field effect are included in the simulation.

3

428

429

430

Amplification processes in gaseous detectors

431 **3.1 Signal formation**

432 **3.2 Gas transport parameters**

4

433

434

Resistive Plate Chambers

435 4.1 Principle

436 4.2 Rate capability of Resistive Plate Chambers

437 4.3 High time resolution

438 4.4 Resistive Plate Chambers at CMS

439 4.4.1 Overview

440 The Resistive Plate Chambers (RPC) system, located in both barrel and endcap
441 regions, provides a fast, independent muon trigger with a looser p_T threshold over
442 a large portion of the pseudorapidity range ($|\eta| < 1.6$) [\[add reconstruction\]](#).

443

444 During High-Luminosity LHC (HL-LHC) operations the expected conditions
445 in terms of background and pile-up will make the identification and correct P_T as-
446 signment a challenge for the Muon system. The goal of RPC upgrade is to provide
447 additional hits to the Muon system with precise timing. All these informations will
448 be elaborated by the trigger system in a global way enhancing the performance of
449 the trigger in terms of efficiency and rate control. The RPC Upgrade is based
450 on two projects: an improved Link Board System and the extension of the RPC
451 coverage up to $|\eta| = 2.4$. [\[FIXME 2.4 or 2.5?\]](#)

452 The Link Board system, that will be described in section xxx, is responsible to
453 process, synchronize and zero-suppress the signals coming from the RPC front end
454 boards. The Link Board components have been produced between 2006 and 2007
455 and will be subjected to aging and failure in the long term. The upgraded Link
456 Board system will overcome the aging problems described in section xxx and will
457 allow for a more precise timing information to the RPC hits from 25 to 1 ns [ref
458 section xxx].

459 The extension of the RPC system up to $|\eta| = 2.1$ was already planned in the
460 CMS TDR [ref cmstdr] and staged because of budget limitations and expected
461 background rates higher than the rate capability of the present CMS RPCs in that
462 region. An extensive R&D program has been done in order to develop an improved
463 RPC that fulfills the CMS requirements. Two new RPC layers in the innermost ring
464 of stations 3 and 4 will be added with benefits to the neutron-induced background
465 reduction and efficiency improvement for both trigger and offline reconstruction.

466 **4.4.2 The present RPC system**

467 The RPC system is organized in 4 stations called RB1 to RB4 in the barrel region,
468 and RE1 to RE4 in the endcap region. The innermost barrel stations, RB1 and
469 RB2, are instrumented with 2 layers of RPCs facing the innermost (RB1in and
470 RB2in) and outermost (RB1out and RB2out) sides of the DT chambers. Every
471 chamber is then divided from the read-out point of view into 2 or 3 η partitions
472 called “rolls”. The RPC system consist of 480 barrel chambers and 576 endcap
473 chambers. Details on the geometry are discussed in the paper [ref to geo paper].

474 The CMS RPC chamber is a double-gap, operated in avalanche mode to ensure
475 reliable operation at high rates. Each RPC gap consists of two 2-mm-thick resistive
476 High-Pressure Laminate (HPL) plates separated by a 2-mm-thick gas gap. The
477 outer surface of the HPL plates is coated with a thin conductive graphite layer, and
478 a voltage is applied. The RPCs are operated with a 3-component, non-flammable
479 gas mixture consisting of 95.2% freon ($C_2H_2F_4$, known as R134a), 4.5% isobutane
480 ($i-C_4H_{10}$), and 0.3% sulphur hexafluoride (SF_6) with a relative humidity of 40% -
481 50%. Readout strips are aligned in η between the 2 gas gaps. [\[Add a sentence on
482 FEBs.\]](#)

483 The discriminated signals coming from the Front End boards feed via twisted
484 cables (10 to 20 m long) the Link Board System located in UXC on the balconies
485 around the detector. The Link System consist of the 1376 Link Boards (LBs)
486 and the 216 Control Boards (CBs), placed in 108 Link Boxes. The Link Box
487 is a custom crate (6U high) with 20 slots (for two CBs and eighteen LBs). The
488 Link Box contains custom backplane to which the cables from the chambers are
489 connected, as well as the cables providing the LBs and CBs power supply and the
490 cables for the RPC FEBs control with use of the I2C protocol (trough the CB). The

491 backplane itself contains only connectors (and no any other electronic devices).
492 The Link Board has 96 input channels (one channel corresponds to one RPC
493 strip). The input signals are the ~ 100 ns binary pulses which are synchronous to
494 the RPC hits, but not to the LHC clock (which drives the entire CMS electronics).
495 Thus the first step of the FEB signals processing is synchronization, i.e. assign-
496 ment of the signals to the BXes (25 ns periods). Then the data are compressed with
497 a simple zero-suppressing algorithm (the input channels are grouped into 8 bit par-
498 titions, only the partitions with at least one nonzero bit are selected for each BX).
499 Next, the non-empty partitions are time-multiplexed i.e. if there are more than one
500 such partition in a given BX, they are sent one-by-one in consecutive BXes. The
501 data from 3 neighbouring LBs are concentrated by the middle LB which contains
502 the optical transmitter for sending them to the USC over a fiber at 1.6 Gbps.

503 The Control Boards provide the communication of the control software with
504 the LBs via the FEC/CCU system. The CBs are connected into token rings, each
505 ring consists of 12 CBs of one detector tower and a FEC mezzanine board placed
506 on the CCS board located in the VME crate in the USC. In total, there are 18 rings
507 in the entire Link System. The CBs also perform automatic reloading of the LB's
508 firmware which is needed in order to avoid accumulation of the radiation induced
509 SEUs in the LBs firmware.

510 Both LBs and CB are based on the Xilinx Spartan III FPGAs, the CB addition-
511 ally contains radiation-tolerant (FLASH based) FPGA Actel ProAsicPlus.

512 The High Voltage power system is located in USC, not exposed to radiation and
513 easily accessible for any reparation. A single HV channel powers 2 RPC chambers
514 both in the barrel and endcap regions. The Low Voltage boards are located in UXC
515 on the balconies and provide the voltage to the front end electronics.

516 **4.4.3 Pulse processing of CMS RPCs**

517 Signals induced by cosmic particle in the RPC strips are shaped by standard CMS
518 RPC Front-End Electronics (FEE) following the scheme of Figure 4.1. On a first
519 stage, analogic signals are amplified and then sent to the Constant Fraction Dis-
520 criminator (CFD) described in Figure 4.2. At the end of the chain, 100 ns long
521 pulses are sent in the LVDS output. These output signal are sent on one side to a
522 V1190A Time-to-Digital Converter (TDC) module from CAEN and on the other
523 to an OR module to count the number of detected signals. Trigger and hit coïnci-
524 dences are monitored using scalers. The TDC is used to store the data into ROOT
525 files. These files are thus analysed to understand the detectors performance.

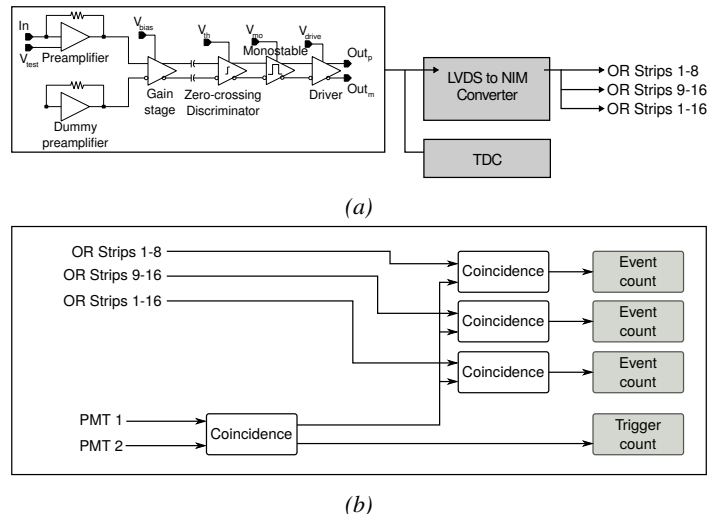


Figure 4.1: Signals from the RPC strips are shaped by the FEE described on Figure 4.1a. Output LVDS signals are then read-out by a TDC module connected to a computer or converted into NIM and sent to scalers. Figure 4.1b describes how these converted signals are put in coincidence with the trigger.

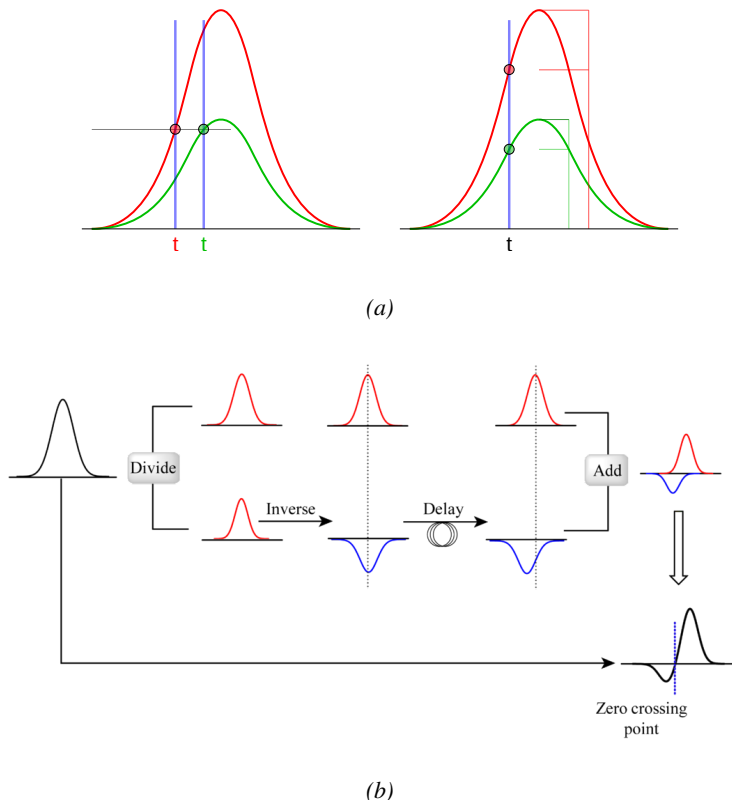


Figure 4.2: Description of the principle of a CFD. A comparison of threshold triggering (left) and constant fraction triggering (right) is shown in Figure 4.2a. Constant fraction triggering is obtained thanks to zero-crossing technique as explained in Figure 4.2b. The signal arriving at the input of the CFD is split into three components. A first one is delayed and connected to the inverting input of a first comparator. A second component is connected to the noninverting input of this first comparator. A third component is connected to the noninverting input of another comparator along with a threshold value connected to the inverting input. Finally, the output of both comparators is fed through an AND gate.

5

526

527 Longevity studies and Consolidation of 528 the present CMS RPC subsystem

529 **5.1 Testing detectors under extreme conditions**

530 The upgrade from LHC to HL-LHC will increase the peak luminosity from 10^{34}
531 $\text{cm}^{-2} \text{s}^{-1}$ to reach $5 \times 10^{34} \text{ cm}^{-2} \text{s}^{-1}$, increasing in the same way the total ex-
532 pected background to which the RPC system will be subjected to. Composed of
533 low energy gammas and neutrons from p - p collisions, low momentum primary
534 and secondary muons, puch-through hadrons from calorimeters, and particles pro-
535 duced in the interaction of the beams with collimators, the background will mostly
536 affect the regions of CMS that are the closest to the beam line, i.e. the RPC detec-
537 tors located in the endcaps. [To update.]

538

539 The 2016 data allowed to study the values of the background rate in all RPC
540 system. In Figure 5.1, the distribution of the chamber background hit rate per unit
541 area is shown at a luminosity of $5 \times 10^{34} \text{ cm}^{-2} \cdot \text{s}^{-1}$ linearly extrapolating from
542 data collected in 2016 [ref mentioning the linear dependency of rate vs lumi]. The
543 maximum rate per unit area at HL-LHC conditions is expected to be of the or-
544 der of 600 Hz/cm^2 (including a safety factor 3). Nevertheless, Fluka simulations
545 have conducted in order to understand the background at HL-LHC conditions. The
546 comparison to the data has shown, in Figure 5.2, a discrepancy of a factor 2 even
547 though the order of magnitude is consistent. [Understand mismatch.]

548

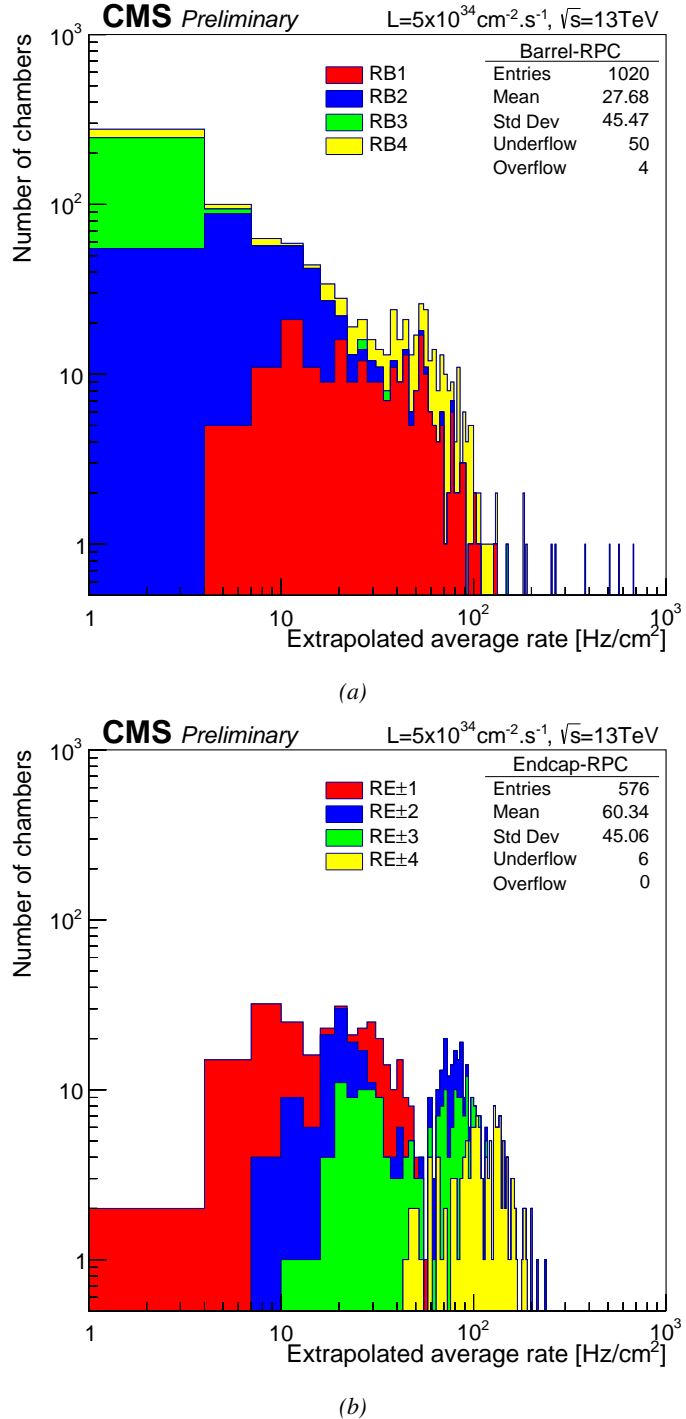


Figure 5.1: (5.1a) Extrapolation from 2016 data of single hit rate per unit area in the barrel region. (5.1b) Extrapolation from 2016 data of single hit rate per unit area in the endcap region.

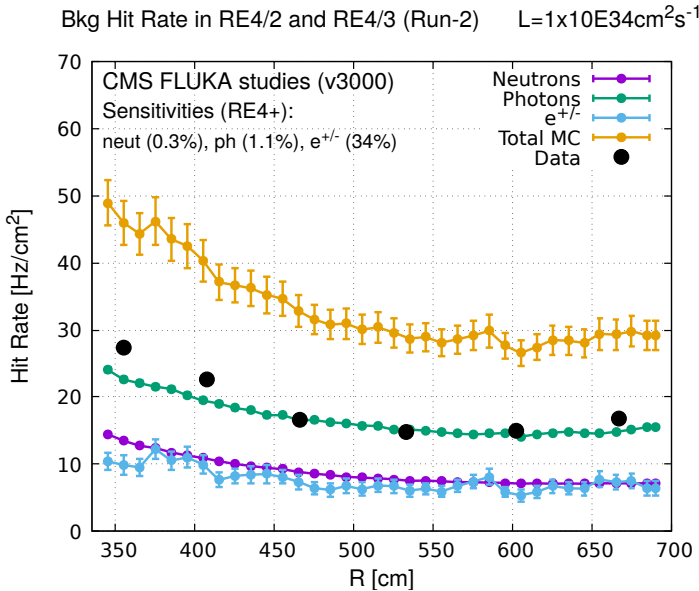


Figure 5.2: Background Fluka simulation compared to 2016 Data at $L = 10^{34} \text{ cm}^{-2} \cdot \text{s}^{-1}$ in the fourth endcap disk region. A mismatch in between simulation and data can be observed. [\[To be understood.\]](#)

549 In the past, extensive long-term tests were carried out at several gamma and
 550 neutron facilities certifying the detector performance. Both full size and small
 551 prototype RPCs have been irradiated with photons up to an integrated charge of
 552 $\sim 0.05 \text{ C}/\text{cm}^2$ and $\sim 0.4 \text{ C}/\text{cm}^2$, respectively [4, 5]. During Run-I, the RPC sys-
 553 tem provided stable operation and excellent performance and did not show any
 554 aging effects for integrated charge of the order of $0.01 \text{ C}/\text{cm}^2$. Projections on cur-
 555 rents from 2016 Data, has allowed to determine that the total integrated charge, by
 556 the end of HL-LHC, would be of the order of $1 \text{ C}/\text{cm}^2$ (including a safety factor
 557 3). [\[Corresponding figure needed.\]](#)

558

559 5.1.1 The Gamma Irradiation Facilities

560 5.1.1.1 GIF

561 Located in the SPS West Area at the downstream end of the X5 test beam, the
 562 Gamma Irradiation Facility (GIF) was a test area in which particle detectors were
 563 exposed to a particle beam in presence of an adjustable gamma background [6].
 564 Its goal was to reproduce background conditions these detectors would suffer in
 565 their operating environment at LHC. GIF layout is shown in Figure 5.3. Gamma

566 photons are produced by a strong ^{137}Cs source installed in the upstream part of the
 567 zone inside a lead container. The source container includes a collimator, designed
 568 to irradiate a $6 \times 6 \text{ m}^2$ area at 5 m maximum to the source. A thin lens-shaped lead
 569 filter helps providing with a uniform outgoing flux in a vertical plane, orthogonal
 570 to the beam direction. The principal collimator hole provides a pyramidal aperture
 571 of $74^\circ \times 74^\circ$ solid angle and provides a photon flux in a pyramidal volume along
 572 the beam axis. The photon rate is controled by further lead filters allowing the
 573 maximum rate to be limited and to vary within a range of four orders of magni-
 574 tude. Particle detectors under test are then placed within the pyramidal volume
 575 in front of the source, perpendicularly to the beam line in order to profit from the
 576 homogeneous photon flux. Adjusting the background flux of photons can then be
 577 done by using the filters and choosing the position of the detectors with respect to
 578 the source.

579

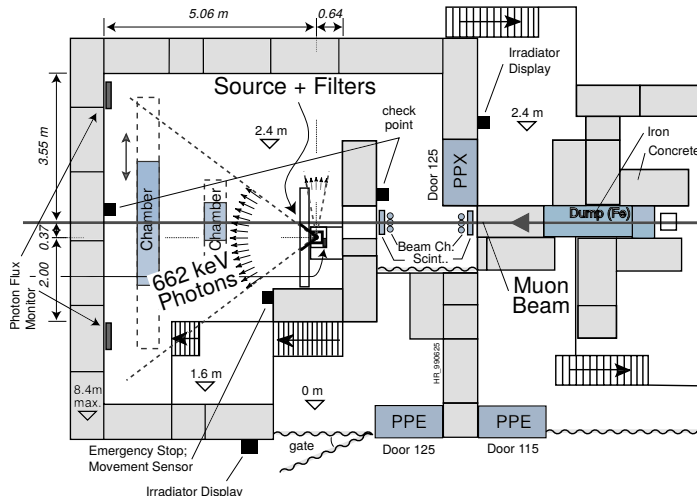


Figure 5.3: Layout of the test beam zone called X5c GIF at CERN. Photons from the radioactive source produce a sustained high rate of random hits over the whole area. The zone is surrounded by 8 m high and 80 cm thick concrete walls. Access is possible through three entry points. Two access doors for personnel and one large gate for material. A crane allows installation of heavy equipment in the area.

580 As described on Figure 5.4, the ^{137}Cs source emits a 662 keV photon in 85%
 581 of the decays. An activity of 740 GBq was measured on the 5th March 1997. To
 582 estimate the strength of the flux in 2014, it is necessary to consider the nuclear
 583 decay through time assiciated to the Cesium source whose half-life is well known
 584 ($t_{1/2} = (30.05 \pm 0.08) \text{ y}$). The GIF tests where done in between the 20th and the
 585 31st of August 2014, i.e. at a time $t = (17.47 \pm 0.02) \text{ y}$ resulting in an attenuation

586 of the activity from 740 GBq in 1997 to 494 GBq in 2014.

587

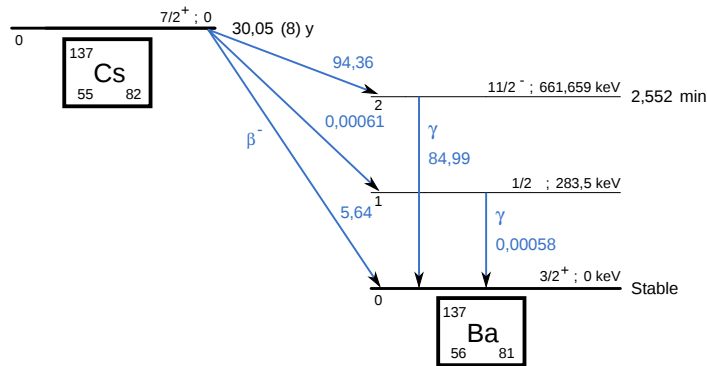


Figure 5.4: ^{137}Cs decays by β^- emission to the ground state of ^{137}Ba (BR = 5.64%) and via the 662 keV isomeric level of ^{137}Ba (BR = 94.36%) whose half-life is 2.55 min.

588 5.1.1.2 GIF++

589 The new Gamma Irradiation Facility (GIF++), located in the SPS North Area at
 590 the downstream end of the H4 test beam, has replaced its predecessor during LS1
 591 and has been operational since spring 2015 [7]. Like GIF, GIF++ features a ^{137}Cs
 592 source of 662 keV gamma photons, their fluence being controlled with a set of
 593 filters of various attenuation factors. The source provides two separated large irra-
 594 diation areas for testing several full-size muon detectors with continuous homoge-
 595 neous irradiation, as presented in Figure 5.5.

596

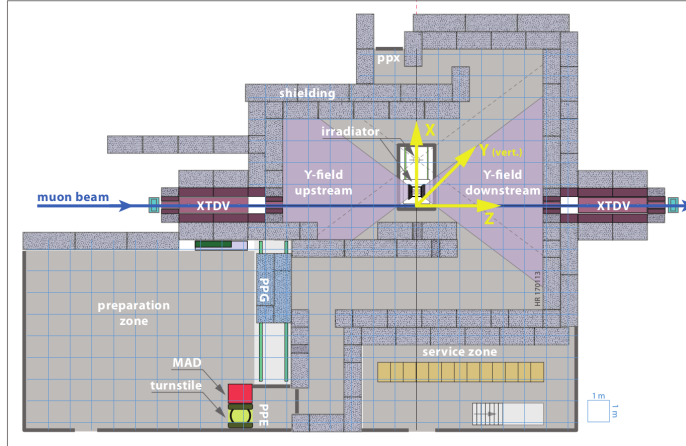


Figure 5.5: Floor plan of the GIF++ facility. When the facility downstream of the GIF++ takes electron beam, a beam pipe is installed along the beam line (z -axis). The irradiator can be displaced laterally (its center moves from $x = 0.65$ m to 2.15 m), to increase the distance to the beam pipe.

597 The source activity was measured to be about 13.5 TBq in March 2016. The
 598 photon flux being far greater than HL-LHC expectations, GIF++ provides an ex-
 599 cellent facility for accelerated aging tests of muon detectors.
 600

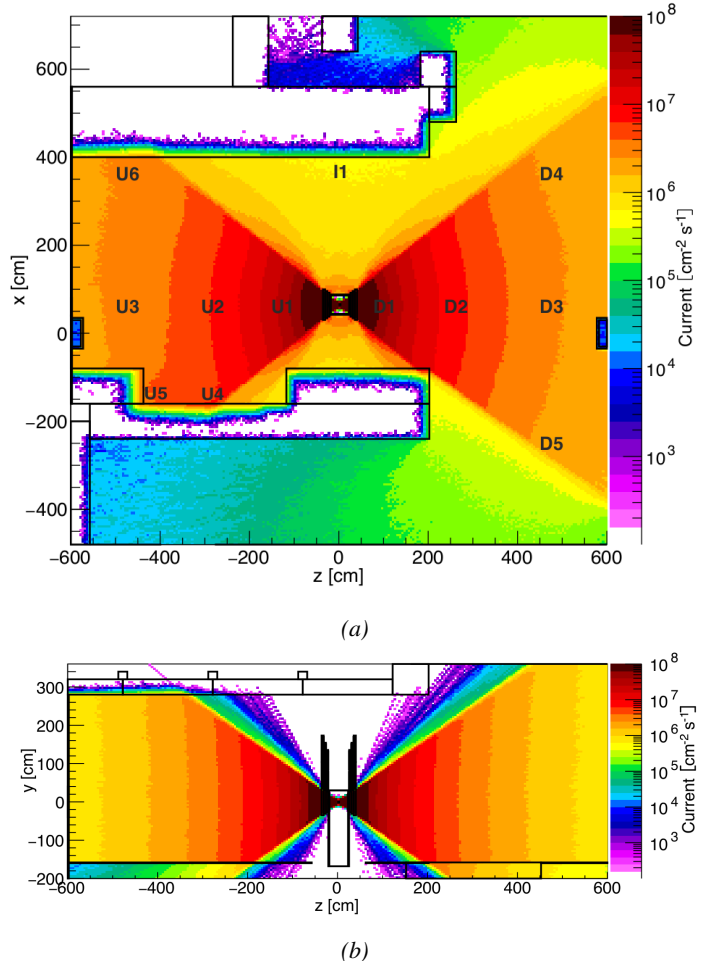


Figure 5.6: Simulated unattenuated current of photons in the xz plane (Figure 5.6a) and yz plane (Figure 5.6b) through the source at $x = 0.65$ m and $y = 0$ m. With angular correction filters, the current of 662 keV photons is made uniform in xy planes.

601 The source is situated in the muon beam line with the muon beam being avail-
 602 able a few times a year. The H4 beam, composed of muons with a momentum of
 603 about 150 GeV/c, passes through the GIF++ zone and is used to study the per-
 604 formance of the detectors. Its flux is of 104 particles/s/cm² focused in an area
 605 similar to 10×10 cm². Therefore, with properly adjusted filters, one can imitate
 606 the HL-LHC background and study the performance of muon detectors with their
 607 trigger/readout electronics in HL-LHC environment.
 608

5.2 Preliminary tests at GIF

5.2.1 Resistive Plate Chamber test setup

During summer 2014, preliminary tests have been conducted in the GIF area on a newly produced RE4/2 chamber labelled RE-4-2-BARC-161. This chamber has been placed into a trolley covered with a tent. The position of the RPC inside the tent and of the tent related to the source is described in Figure 5.7. To test this CMS RPC, three different absorber settings were used. First of all, measurements were done with fully opened source. Then, to complete this preliminary study, the gamma flux has been attenuated from a factor 2 and a factor 5. The expected gamma flux at the level of our detector will be discussed in subsection 5.2.4.

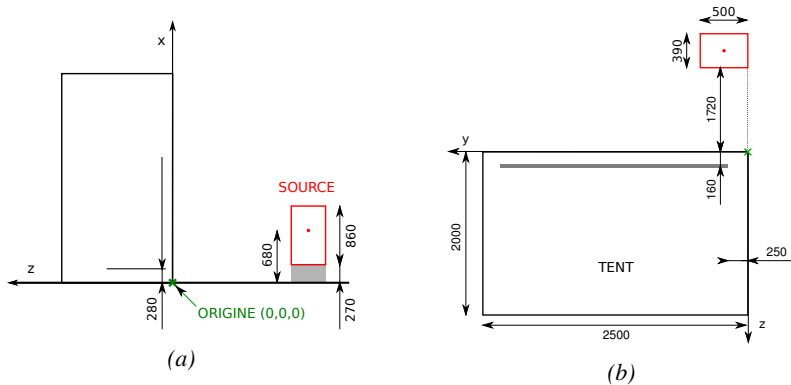


Figure 5.7: Description of the RPC setup. Dimensions are given in mm. A tent containing RPCs is placed at 1720 mm from the source container. The source is situated in the center of the container. RE-4-2-BARC-161 chamber is 160 mm inside the tent. This way, the distance between the source and the chambers plan is 2060 mm. Figure 5.7a provides a side view of the setup in the xz plane while Figure 5.7b shows a top view in the yz plane.



Figure 5.8: RE-4-2-BARC-161 chamber is inside the tent as described in Figure 5.7. In the top right, the two scintillators used as trigger can be seen. This trigger system has an inclination of 10° relative to horizontal and is placed above half-partition B2 of the RPCs. PMT electronics are shielded thanks to lead blocks placed in order to protect them without stopping photons from going through the scintillators and the chamber.

619 At the time of the tests, the beam not being operational anymore, a trigger
620 composed of 2 plastic scintillators has been placed in front of the setup with an
621 inclination of 10 deg with respect to the detector plane in order to look at cosmic
622 muons. Using this particular trigger layout, shown on Figure 5.8, leads to a cosmic
623 muon hit distribution into the chamber similar to the one in Figure 5.9. Measured
624 without gamma irradiation, two peaks can be seen on the profil of partition B, cen-
625 tered on strips 52 and 59. Section 5.2.3 will help us understand that these two peaks
626 are due respectively to forward and backward coming cosmic particles where for-
627 ward coming particles are first detected by the scintillators and then the RPC while
628 the backward coming muons are first detected in the RPC.

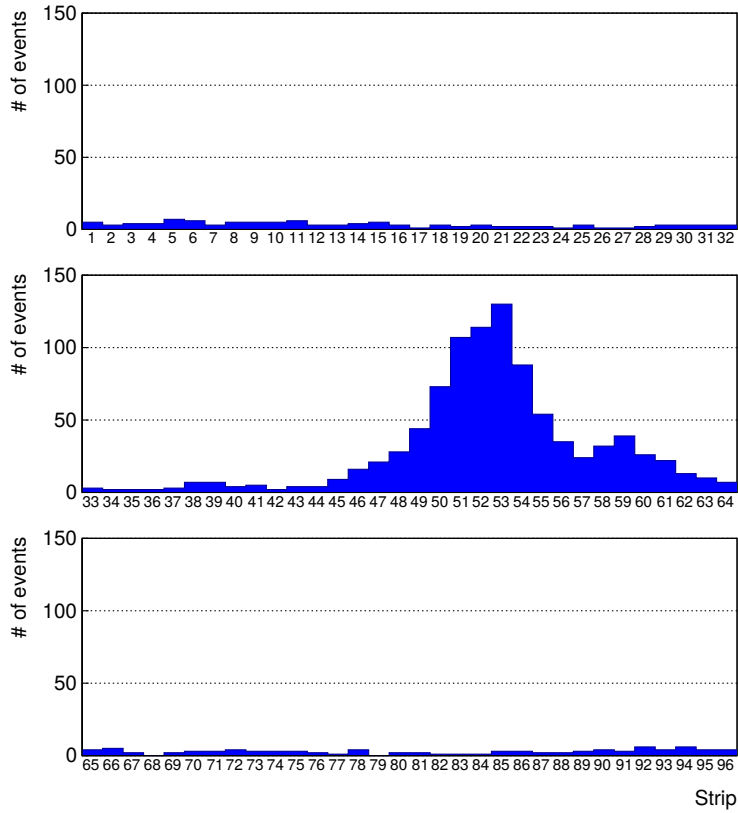


Figure 5.9: Hit distributions over all 3 partitions of RE-4-2-BARC-161 chamber is showed on these plots. Top, middle and bottom figures respectively correspond to partitions A, B, and C. These plots show that some events still occur in other half-partitions than B2, which corresponds to strips 49 to 64, in front of which the trigger is placed, contributing to the inefficiency of detection of cosmic muons. In the case of partitions A and C, the very low amount of data can be interpreted as noise. On the other hand, it is clear that a little portion of muons reach the half-partition B1, corresponding to strips 33 to 48.

629 5.2.2 Data Acquisition

630 5.2.3 Geometrical acceptance of the setup layout to cosmic muons

631 In order to profit from a constant gamma irradiation, the detectors inside of the GIF
 632 bunker need to be placed in a plane orthogonal to the beam line. The muon beam
 633 that used to be available was meant to test the performance of detectors under test.
 634 This beam not being active anymore, another solution to test detector performance
 635 had to be used. Thus, it has been decided to use cosmic muons detected through

636 a telescope composed of two scintillators. Lead blocks were used as shielding to
 637 protect the photomultipliers from gammas as can be seen from Figure 5.8.

638 An inclination has been given to the cosmic telescope to maximize the muon
 639 flux. A good compromise had to be found between good enough muon flux and
 640 narrow enough hit distribution to be sure to contain all the events into only one half
 641 partitions as required from the limited available readout hardware. Nevertheless,
 642 a consequence of the misplaced trigger, that can be seen as a loss of events in
 643 half-partition B1 in Figure 5.9, is an inefficiency. Nevertheless, the inefficiency
 644 of approximately 20 % highlighted in Figure 5.10 by comparing the performance
 645 of chamber BARC-161 in 904 and at GIF without irradiation seems too important
 646 to be explained only by the geometrical acceptance of the setup itself. Simulations
 647 have been conducted to show how the setup brings inefficiency.

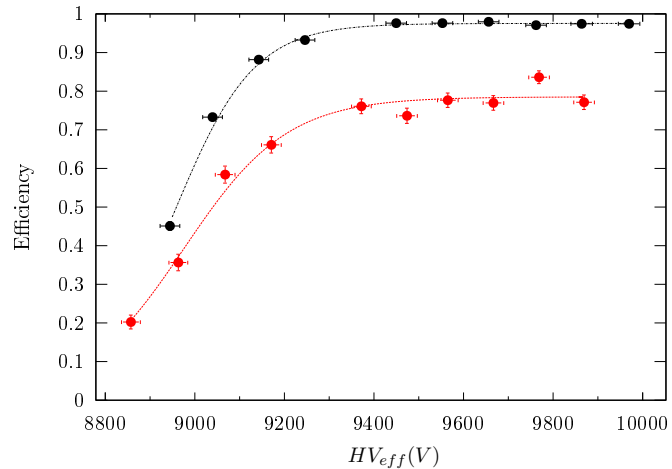


Figure 5.10: Results are derived from data taken on half-partition B2 only. On the 18th of June 2014, data has been taken on chamber RE-2-BARC-161 at building 904 (Prevessin Site) with cosmic muons providing us a reference efficiency plateau of $(97.54 \pm 0.15)\%$ represented by a black curve. A similar measurement has been done at GIF on the 21st of July with the same chamber giving a plateau of $(78.52 \pm 0.94)\%$ represented by a red curve.

648 5.2.3.1 Description of the simulation layout

649 The layout of GIF setup has been reproduced and incorporated into a Monte Carlo
 650 (MC) simulation to study the influence of the disposition of the telescope on the
 651 final distribution measured by the RPC. A 3D view of the simulated layout is given
 652 into Figure 5.11. Muons are generated randomly in a horizontal plane located at a
 653 height corresponding to the lowest point of the PMTs. This way, the needed size
 654 of the plane in order to simulate events happening at very big azimuthal angles (i.e.

655 $\theta \approx \pi$) can be kept relatively small. The muon flux is designed to follow the usual
 656 $\cos^2\theta$ distribution for cosmic particle. The goal of the simulation is to look at
 657 muons that pass through the muon telescope composed of the two scintillators and
 658 define their distribution onto the RPC plane. During the reconstruction, the RPC
 659 plane is then divided into its strips and each muon track is assigned to a strip.

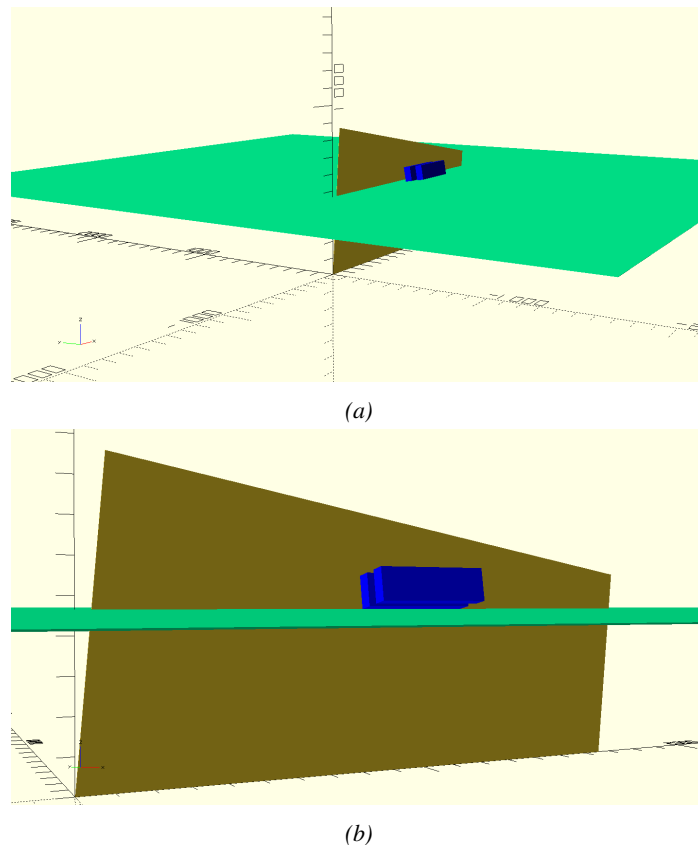


Figure 5.11: Representation of the layout used for the simulations of the test setup. The RPC is represented as a yellow trapezoid while the two scintillators as blue cuboids looking at the sky. A green plane corresponds to the muon generation plane within the simulation. Figure 5.7a shows a global view of the simulated setup. Figure 5.7b shows a zoomed view that allows to see the 2 scintillators as well as the full RPC plane.

660 In order to further refine the quality of the simulation and understand deeper
 661 the results the dependance of the distribution has been studied for a range of tele-
 662 scope inclinations. Moreover, the threshold applied on the PMT signals has been
 663 included into the simulation in the form of a cut. In the approximation of uni-
 664 form scintillators, it has been considered that the threshold can be understood as

665 the minimum distance particles need to travel through the scintillating material to
666 give a strong enough signal. Particles that travel a distance smaller than the set
667 "threshold" are thus not detected by the telescope and cannot trigger the data tak-
668 ing. Finally, the FEE threshold also has been considered in a similar way. The
669 mean momentum of horizontal cosmic rays is higher than those of vertical ones
670 but the stopping power of matter for momenta ranging from 1 GeV to 1 TeV stays
671 comparable. It is then possible to assume that the mean number of primary e^-/ion
672 pairs per unit length will stay similar and thus, depending on the applied discrimi-
673 nator threshold, muons with the shortest path through the gas volume will deposit
674 less charge and induce a smaller signal on the pick-up strips that could eventu-
675 ally not be detected. These two thresholds also restrain the overall geometrical
676 acceptance of the system.

677 **5.2.3.2 Simulation procedure**

678 The simulation software has been designed using C++ and the output data is saved
679 into ROOT histograms. Simulations start for a threshold T_{scint} varying in a range
680 from 0 to 45 mm in steps of 5 mm, where $T_{scint} = 0 \text{ mm}$ corresponds to the case
681 where there isn't any threshold apply on the input signal while $T_{scint} = 45 \text{ mm}$,
682 which is the scintillator thickness, is the case where muons cannot arrive orthogo-
683 nally onto the scintillator surface. For a given T_{scint} , a set of RPC thresholds are
684 considered. The RPC threshold, T_{RPC} varies from 2 mm, the thickness of the gas
685 volume, to 3 mm in steps of 0.25 mm. For each $(T_{scint}; T_{RPC})$ pair, $N_\mu = 10^8$
686 muons are randomly generated inside the muon plane described in the previous
687 paragraph with an azimuthal angle θ chosen to follow a $\cos^2\theta$ distribution.

688 Planes are associated to each surface of the scintillators. Knowing muon posi-
689 tion into the muon plane and its direction allows us, by assuming that muons travel
690 in a straight line, to compute the intersection of the muon track with these planes.
691 Applying conditions to the limits of the surfaces of the scintillator faces then gives
692 us an answer to whether or not the muon passed through the scintillators. In the
693 case the muon has indeed passed through the telescope, the path through each scin-
694 tillator is computed and muons whose path was shorter than T_{scint} are rejected and
695 are thus considered as having not interacted with the setup.

696 On the contrary, if the muon is labeled as good, its position within the RPC
697 plane is computed and the corresponding strip, determined by geometrical tests
698 in the case the distance through the gas volume was enough not to be rejected
699 because of T_{RPC} , gets a hit and several histograms are filled in order to keep
700 track of the generation point on the muon plane, the intersection points of the
701 reconstructed muons within the telescope, or on the RPC plane, the path traveled
702 through each individual scintillator or the gas volume, as well as other histograms.
703 Moreover, muons fill different histograms whether they are forward or backward
704 coming muons. They are discriminated according to their direction components.

705 When a muon is generated, an (x, y, z) position is assigned into the muon plane as
 706 well as a $(\theta; \phi)$ pair that gives us the direction it's coming from. This way, muons
 707 satisfying the condition $0 \leq \phi < \pi$ are designated as backward coming muons
 708 while muons satisfying $\pi \leq \phi < 2\pi$ as forward coming muons.

709 This simulation is then repeated for different telescope inclinations ranging in
 710 between 4 and 20° and varying in steps of 2° . Due to this inclination and to the
 711 vertical position of the detector under test, the muon distribution reconstructed in
 712 the detector plane is asymmetrical. The choice has been made to chose a skew
 713 distribution formula to fit the data built as the multiplication of gaussian and sig-
 714 moidal curves together. A typical gaussian formula is given as 5.1 and has three
 715 free parameters as A_g , its amplitude, \bar{x} , its mean value and σ , its root mean square.
 716 Sigmoidal curves as given by formula 5.2 are functions converging to 0 and A_s as
 717 x diverges. The inflexion point is given as x_i and λ is proportional to the slope at
 718 $x = x_i$. In the limit where $\lambda \rightarrow \infty$, the sigmoid becomes a step function.

$$g(x) = A_g e^{\frac{-(x-\bar{x})^2}{2\sigma^2}} \quad (5.1)$$

$$s(x) = \frac{A_s}{1 + e^{-\lambda(x-x_i)}} \quad (5.2)$$

719 Finally, a possible representation of a skew distribution is given by formula 5.3
 720 and is the product of 5.1 and 5.2. Naturally, here $A_{sk} = A_g \times A_s$ and represents
 721 the theoretical maximum in the limit where the skew tends to a gaussian function.

$$sk(x) = g(x) \times s(x) = A_{sk} \frac{e^{\frac{-(x-\bar{x})^2}{2\sigma^2}}}{1 + e^{-\lambda(x-x_i)}} \quad (5.3)$$

722 5.2.3.3 Results

723 Influence of T_{scint} on the muon distribution

724 Influence of T_{RPC} on the muon distribution

725 Influence of the telescope inclination on the muon distribution

726 Comparison to data taken at GIF without irradiation

727 **5.2.4 Photon flux at GIF**

728 **5.2.4.1 Expectations from simulations**

729 In order to understand and evaluate the γ flux in the GIF area, simulations had been
 730 conducted in 1999 and published by S. Agosteo et al [6]. Table 5.1 presented in
 731 this article gives us the γ flux for different distances D to the source. This sim-
 732 ulation was done using GEANT and a Monte Carlo N-Particle (MCNP) transport
 733 code, and the flux F is given in number of γ per unit area and unit time along with
 734 the estimated error from these packages expressed in %.

Nominal ABS	Photon flux F [$s^{-1}cm^{-2}$]			
	at $D = 50$ cm	at $D = 155$ cm	at $D = 300$ cm	at $D = 400$ cm
1	$0.12 \cdot 10^8 \pm 0.2\%$	$0.14 \cdot 10^7 \pm 0.5\%$	$0.45 \cdot 10^6 \pm 0.5\%$	$0.28 \cdot 10^6 \pm 0.5\%$
2	$0.68 \cdot 10^7 \pm 0.3\%$	$0.80 \cdot 10^6 \pm 0.8\%$	$0.25 \cdot 10^6 \pm 0.8\%$	$0.16 \cdot 10^6 \pm 0.6\%$
5	$0.31 \cdot 10^7 \pm 0.4\%$	$0.36 \cdot 10^6 \pm 1.2\%$	$0.11 \cdot 10^6 \pm 1.2\%$	$0.70 \cdot 10^5 \pm 0.9\%$

Table 5.1: Total photon flux ($E\gamma \leq 662$ keV) with statistical error predicted considering a ^{137}Cs activity of 740 GBq at different values of the distance D to the source along the x-axis of irradiation field [6].

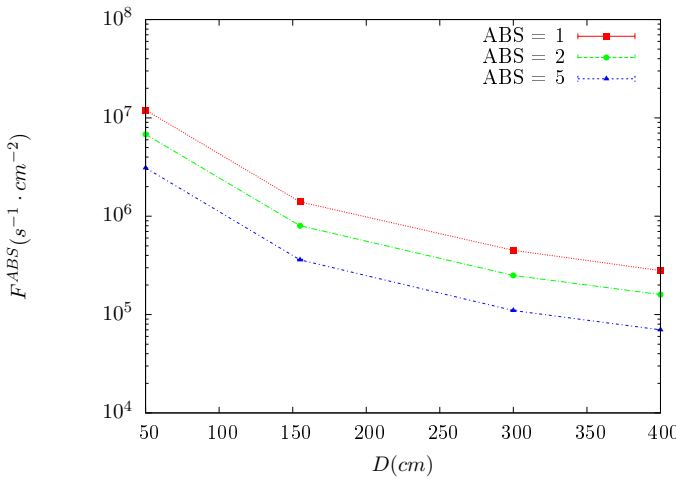


Figure 5.12: γ flux $F(D)$ is plot using values from table 5.1. As expected, the plot shows similar attenuation behaviours with increasing distance for each absorption factors.

735 The simulation doesn't directly provides us with an estimated flux at the level
 736 of our RPC. First of all, it is needed to extract the value of the flux from the
 737 available data contained in the original paper and then to estimate the flux in 2014
 738 at the time the experimentation took place. Figure 5.12 that contains the data from

739 Table 5.1. In the case of a pointlike source emitting isotropic and homogeneous
 740 gamma radiations, the gamma flux F at a distance D to the source with respect
 741 to a reference point situated at D_0 where a known flux F_0 is measured will be
 742 expressed like in Equation 5.4, assuming that the flux decreases as $1/D^2$, where c
 743 is a fitting factor.

$$F^{ABS} = F_0^{ABS} \times \left(\frac{cD_0}{D} \right)^2 \quad (5.4)$$

744 By rewriting Equation 5.4, it comes that :

$$c = \frac{D}{D_0} \sqrt{\frac{F^{ABS}}{F_0^{ABS}}} \quad (5.5)$$

$$\Delta c = \frac{c}{2} \left(\frac{\Delta F^{ABS}}{F^{ABS}} + \frac{\Delta F_0^{ABS}}{F_0^{ABS}} \right) \quad (5.6)$$

745 Finally, using Equation 5.5 and the data in Table 5.1 with $D_0 = 50$ cm as
 746 reference point, we can build Table 5.2. It is interesting to note that c for each
 747 value of D doesn't depend on the absorption factor.

Nominal ABS	Correction factor c		
	at $D = 155$ cm	at $D = 300$ cm	at $D = 400$ cm
1	$1.059 \pm 0.70\%$	$1.162 \pm 0.70\%$	$1.222 \pm 0.70\%$
2	$1.063 \pm 1.10\%$	$1.150 \pm 1.10\%$	$1.227 \pm 0.90\%$
5	$1.056 \pm 1.60\%$	$1.130 \pm 1.60\%$	$1.202 \pm 1.30\%$

Table 5.2: Correction factor c is computed thanks to formulae 5.5 taking as reference $D_0 = 50$ cm and the associated flux F_0^{ABS} for each absorption factor available in table 5.1.

748 For the range of D/D_0 values available, it is possible to use a simple linear
 749 fit to get the evolution of c . The linear fit will then use only 2 free parameters, a
 750 and b , as written in Equation 5.7. This gives us the results showed in Figure 5.13.
 751 Figure 5.13b confirms that using only a linear fit to extract c is enough as the
 752 evolution of the rate that can be obtained superimposes well on the simulation
 753 points.

$$c \left(\frac{D}{D_0} \right) = a \frac{D}{D_0} + b \quad (5.7)$$

$$F^{ABS} = F_0^{ABS} \left(a + \frac{bD_0}{D} \right)^2 \quad (5.8)$$

$$\Delta F^{ABS} = F^{ABS} \left[\frac{\Delta F_0^{ABS}}{F_0^{ABS}} + 2 \frac{\Delta a + \Delta b \frac{D_0}{D}}{a + \frac{bD_0}{D}} \right] \quad (5.9)$$

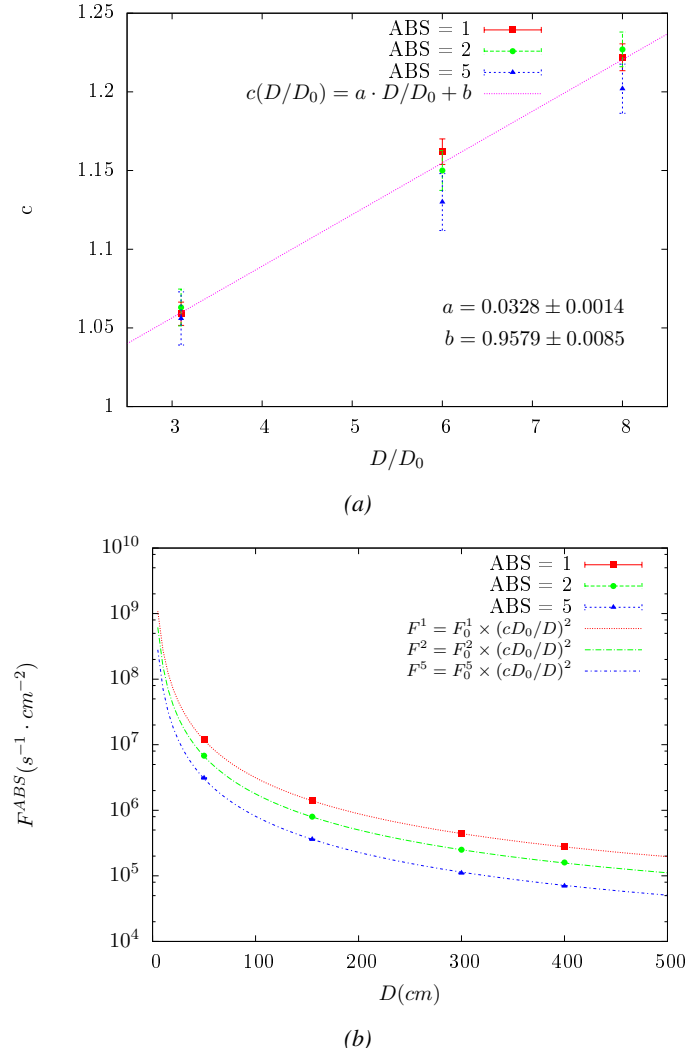


Figure 5.13: Figure 5.13a shows the linear approximation fit done via formulae 5.7 on data from table 5.2. Figure 5.13b shows a comparison of this model with the simulated flux using a and b given in figure 5.13a in formulae 5.4 and the reference value $D_0 = 50\text{cm}$ and the associated flux for each absorption factor F_0^{ABS} from table 5.1

In the case of the 2014 GIF tests, the RPC plane is located at a distance $D = 206\text{ cm}$ to the source. Moreover, to estimate the strength of the flux in 2014, it is necessary to consider the nuclear decay through time associated to the Cesium source whose half-life is well known ($t_{1/2} = (30.05 \pm 0.08)\text{ y}$). The very first source activity measurement has been done on the 5th of March 1997 while the

759 GIF tests were done between the 20th and the 31st of August 2014, i.e. at a
 760 time $t = (17.47 \pm 0.02)$ y resulting in an attenuation of the activity from 740 GBq
 761 in 1997 to 494 GBq in 2014. All the needed information to extrapolate the flux
 762 through our detector in 2014 has now been assembled, leading to the Table 5.3. It
 763 is interesting to note that for a common RPC sensitivity to γ of $2 \cdot 10^{-3}$, the order
 764 of magnitude of the estimated hit rate per unit area is of the order of the kHz for
 765 the fully opened source. Moreover, taking profit of the two working absorbers, it
 766 will be possible to scan background rates at 0 Hz, ~ 300 Hz as well as ~ 600 Hz.
 767 Without source, a good estimate of the intrinsic performance will be available.
 768 Then at 300 Hz, the goal will be to show that the detectors fulfill the performance
 769 certification of CMS RPCs. Then a first idea of the performance of the detectors at
 770 higher background will be provided with absorption factors 2 (~ 600 Hz) and 1 (no
 771 absorption). *[Here I will also put a reference to the plot showing the estimated
 772 background rate at the level of RE3/I in the case of HL-LHC but this one being
 773 in another chapter, I will do it later.]*

Nominal ABS	Photon flux F [$s^{-1}cm^{-2}$]			Hit rate/unit area [$Hz cm^{-2}$] at $D^{2014} = 206$ cm
	at $D_0^{1997} = 50$ cm	at $D^{1997} = 206$ cm	at $D^{2014} = 206$ cm	
1	$0.12 \cdot 10^8 \pm 0.2\%$	$0.84 \cdot 10^6 \pm 0.3\%$	$0.56 \cdot 10^6 \pm 0.3\%$	1129 ± 32
2	$0.68 \cdot 10^7 \pm 0.3\%$	$0.48 \cdot 10^6 \pm 0.3\%$	$0.32 \cdot 10^6 \pm 0.3\%$	640 ± 19
5	$0.31 \cdot 10^7 \pm 0.4\%$	$0.22 \cdot 10^6 \pm 0.3\%$	$0.15 \cdot 10^6 \pm 0.3\%$	292 ± 9

Table 5.3: The data at D_0 in 1997 is taken from [6]. In a second step, using Equations 5.8 and 5.9, the flux at D can be estimated in 1997. Then, taking into account the attenuation of the source activity, the flux at D can be estimated at the time of the tests in GIF in 2014. Finally, assuming a sensitivity of the RPC to γ $s = 2 \cdot 10^{-3}$, an estimation of the hit rate per unit area is obtained.

774 **5.2.4.2 Dose measurements**

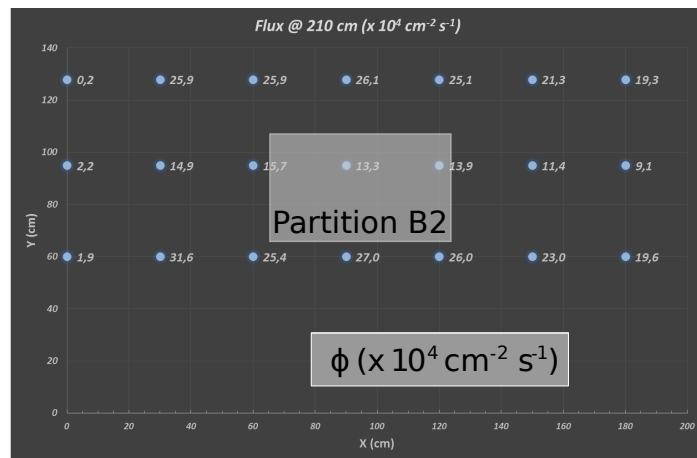


Figure 5.14: Dose measurements has been done in a plane corresponding to the tents front side. This plan is 1900 mm away from the source. As explained in the first chapter, a lens-shaped lead filter provides a uniform photon flux in the vertical plan orthogonal to the beam direction. If the second line of measured fluxes is not taken into account because of lower values due to experimental equipments in the way between the source and the tent, the uniformity of the flux is well showed by the results.

775 5.2.5 Results and discussions

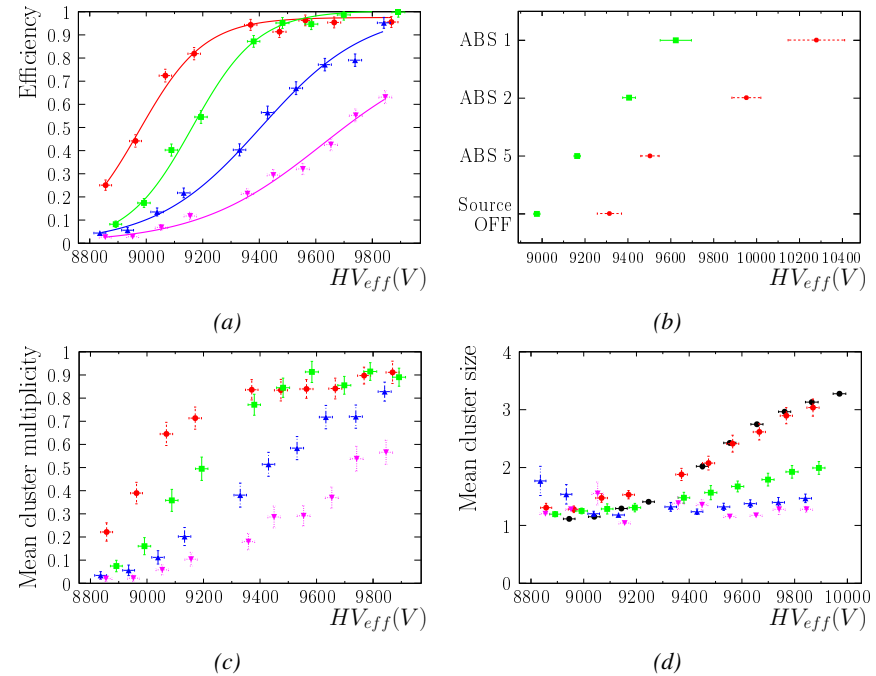


Figure 5.15

5.3 Longevity tests at GIF++

776 Longevity studies imply a monitoring of the performance of the detectors probed
777 using a high intensity muon beam in a irradiated environment by periodically mea-
778 suring their rate capability, the dark current running through them and the bulk
779 resistivity of the Bakelite composing their electrodes. GIF++, with its very intense
780 ^{137}Cs source, provides the perfect environment to perform such kind of tests. As-
781 suming a maximum acceleration factor of 3, it is expected to accumulate the equiv-
782 alent charge in 1.7 years.

783 As the maximum background is found in the endcap, the choice naturally was
784 made to focus the GIF++ longevity studies on endcap chambers. Most of the RPC
785 system was installed in 2007. Nevertheless, the large chambers in the fourth end-
786 cap (RE4/2 and RE4/3) have been installed during LS1 in 2014. The Bakelite of
787 these two different productions having different properties, four spare chambers
788 of the present system were selected, two RE2,3/2 spares and two RE4/2 spares.
789 Having two chambers of each type allows to always keep one of them non irradia-
790 ted as reference, the performance evolution of the irradiated chamber being then
791 compared through time to the performance of the non irradiated one.

792 The performance of the detectors under different level of irradiation is measured
793 periodically during dedicated test beam periods using the H4 muon beam. In be-
794 tween these test beam periods, the two RE2,3/2 and RE4/2 chambers selected for
795 this study are irradiated by the ^{137}Cs source in order to accumulate charge and
796 the gamma background is monitored, as well as the currents. The two remaining
797 chambers are kept non-irradiated as reference detectors. Due to the limited gas
798 flow in GIF++, the RE4 chamber remained non-irradiated until end of November
799 2016 where a new mass flow controller has been installed allowing for bigger vol-
800 umes of gas to flow in the system.

801 Figures 5.16 and 5.17 give us for different test beam periods, and thus for in-
802 creasing integrated charge through time, a comparison of the maximum efficiency,
803 obtained using a sigmoid-like function, and of the working point of both irradiated
804 and non irradiated chambers [8]. No aging is yet to see from this data, the shifts in
805 γ rate per unit area in between irradiated and non irradiated detectors and RE2 and
806 RE4 types being easily explained by a difference of sensitivity due to the various
807 Bakelite resistivities of the HPL electrodes used for the electrode production.

808 Collecting performance data at each test beam period allows us to extrapolate the
809 maximum efficiency for a background hit rate of 300 Hz/cm^2 corresponding to
810 the expected HL-LHC conditions. Aging effects could emerge from a loss of ef-
811 ficiency with increasing integrated charge over time, thus Figure 5.18 helps us
812 understand such degradation of the performance of irradiated detectors in compar-
813 ison with non irradiated ones. The final answer for an eventual loss of efficiency is
814 given in Figure 5.19 by comparing for both irradiated and non irradiated detectors

816 the efficiency sigmoids before and after the longevity study. Moreover, to complete
 817 the performance information, the Bakelite resistivity is regularly measured thanks
 818 to Ag scans (Figure 5.20) and the noise rate is monitored weekly during irradiation
 819 periods (Figure 5.21). At the end of 2016, no signs of aging were observed and
 820 further investigation is needed to get closer to the final integrated charge require-
 821 ments proposed for the longevity study of the present CMS RPC sub-system.

822

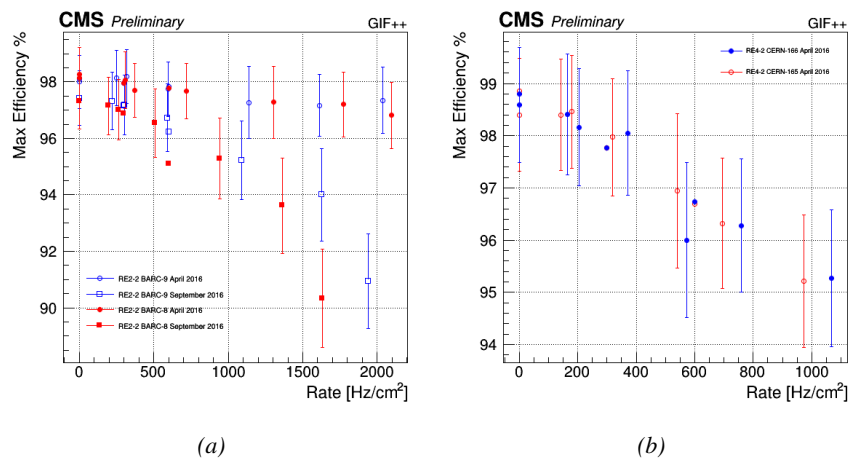


Figure 5.16: Evolution of the maximum efficiency for RE2 (5.16a) and RE4 (5.16b) chambers with increasing extrapolated γ rate per unit area at working point. Both irradiated (blue) and non irradiated (red) chambers are shown.

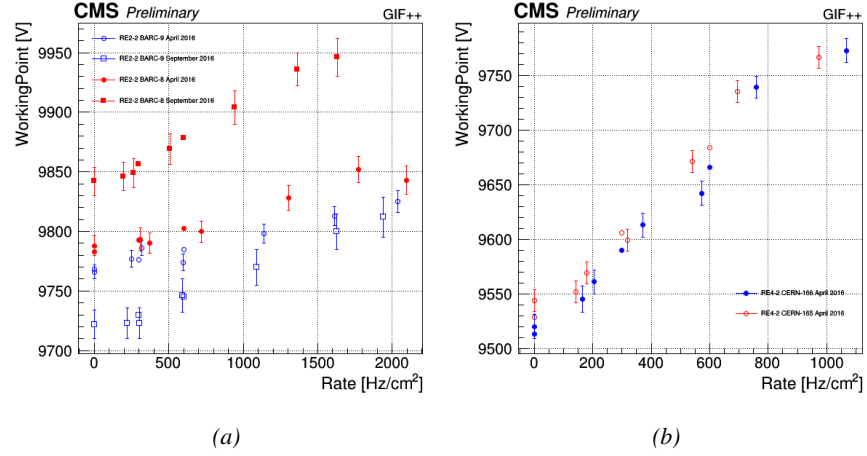


Figure 5.17: Evolution of the working point for RE2 (5.17a) and RE4 (5.17b) with increasing extrapolated γ rate per unit area at working point. Both irradiated (blue) and non irradiated (red) chambers are shown.

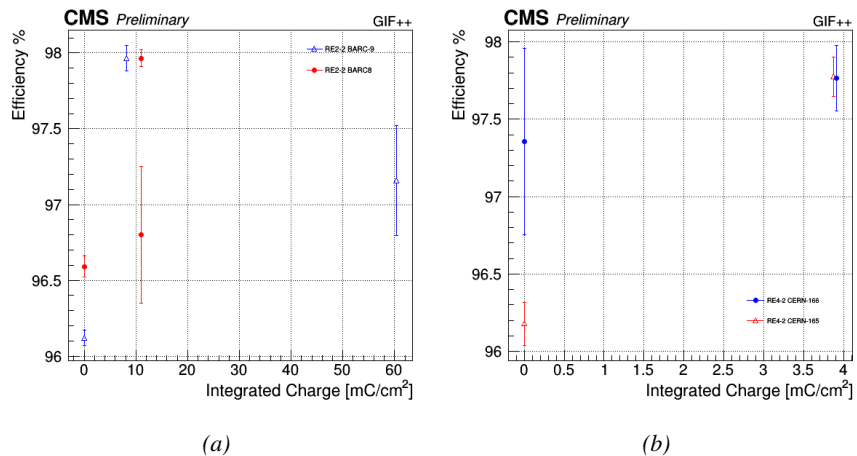


Figure 5.18: Evolution of the maximum efficiency at HL-LHC conditions, i.e. a background hit rate per unit area of 300 Hz/cm², with increasing integrated charge for RE2 (5.18a) and RE4 (5.18b) detectors. Both irradiated (blue) and non irradiated (red) chambers are shown. The integrated charge for non irradiated detectors is recorded during test beam periods and stays small with respect to the charge accumulated in irradiated chambers.

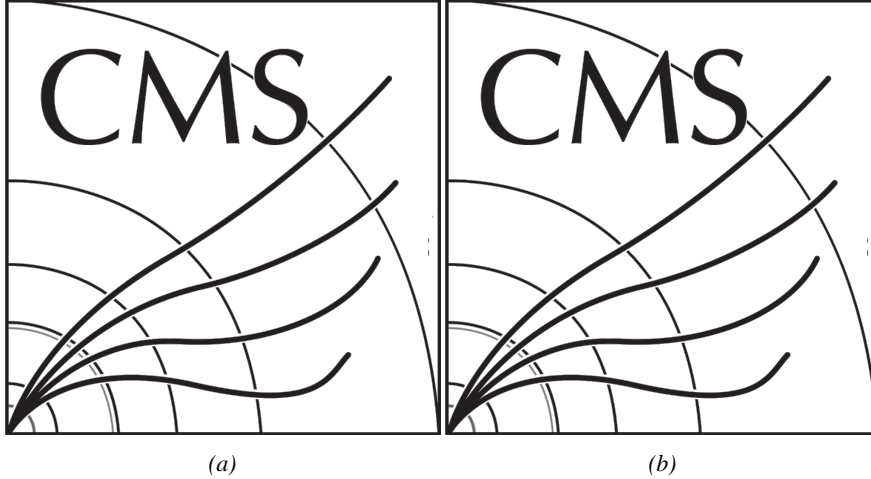


Figure 5.19: Comparison of the efficiency sigmoid before (triangles) and after (circles) irradiation for RE2 (5.19a) and RE4 (5.19b) detectors. Both irradiated (blue) and non irradiated (red) chambers are shown.

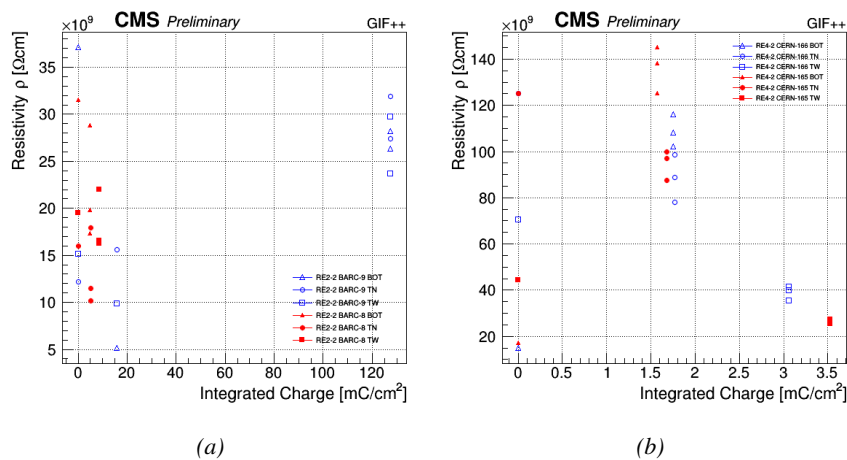


Figure 5.20: Evolution of the Bakelite resistivity for RE2 (5.20a) and RE4 (5.20b) detectors. Both irradiated (blue) and non irradiated (red) chambers are shown.

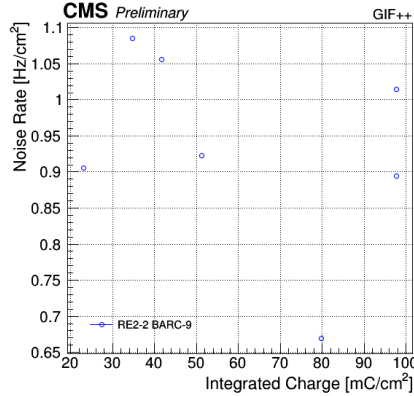


Figure 5.21: Evolution of the noise rate per unit area for the irradiated chamber RE2-2-BARC-9 only.

5.3.1 Description of the Data Acquisition

For the longevity studies, four spare chambers of the present system are used. Two spare RPCs of the RE2,3 stations as well as two spare RPCs from the new RE4 stations have been mounted in a Trolley. Six RE4 gaps are also placed in the trolley. The trolley is placed inside the GIF++ in the upstream region of the bunker, taking the cesium source as a reference. The trolley is oriented for the detection surface of the chambers to be orthogonal to the beam line. The system can be moved along the orthogonal plane in order to have the beam in all η -partitions. For the aging the trolley is moved outside the beam line and is placed in a distance of 5.2 m to the source, which irradiates the bunker using an attenuation filter of 2.2 which corresponds to a fluence of 10^7 gamma/cm².

During GIF++ operation, the data collected can be divided into different categories as several parameters are monitored in addition to the usual RPC performance data. On one hand, to know the performance of a chamber, it is need to measure its efficiency and to know the background conditions in which it is operated. To do this, the hit signals from the chamber are recorded and stored in a ROOT file via a Data Acquisition (DAQ) software. On the other hand, it is also very important to monitor parameters such as environmental pressure and temperature, gas temperature and humidity, RPC HV, LV, and currents, or even source and beam status. This is done through the GIF++ web Detector Control Software (DCS) that stores this information in a database.

Two different types of tests are conducted on RPCs via the DAQ. Indeed, the performance of the detectors is measured periodically during dedicated test beam periods using the H4 muon beam. In between these test beam periods, when the beam is not available, the chambers are irradiated by the ^{137}Cs in order to accu-

848 mulate deposited charge and the gamma background is measured.

849 RPCs under test are connected through LVDS cables to V1190A Time-to-
 850 Digital Converter (TDC) modules manufactured by CAEN. These modules, lo-
 851 cated in the rack area outside of the bunker, get the logic signals sent by the cham-
 852 bers and save them into their buffers. Due to the limited size of the buffers, the
 853 collected data is regularly erased and replaced. A trigger signal is needed for the
 854 TDC modules to send the useful data to the DAQ computer via a V1718 CAEN
 855 USB communication module.

856 In the case of performance test, the trigger signal used for data acquisition is
 857 generated by the coincidence of three scintillators. A first one is placed upstream
 858 outside of the bunker, a second one is placed downstream outside of the bunker,
 859 while a third one is placed in front of the trolley, close by the chambers. Every time
 860 a trigger is sent to the TDCs, i.e. every time a muon is detected, knowing the time
 861 delay in between the trigger and the RPC signals, signals located in the right time
 862 window are extracted from the buffers and saved for later analysis. Signals are
 863 taken in a time window of 400 ns centered on the muon peak (here we could show
 864 a time spectrum). On the other hand, in the case of background rate measurement,
 865 the trigger signal needs to be "random" not to measure muons but to look at gamma
 866 background. A trigger pulse is continuously generated at a rate of 300 Hz using a
 867 dual timer. To integrate an as great as possible time, all signals contained within
 868 a time window of 10us prior to the random trigger signal are extracted form the
 869 buffers and saved for further analysis (here another time spectrum to illustrate
 870 could be useful, maybe even place both spectrum together as a single Figure).

871 The signals sent to the TDCs correspond to hit collections in the RPCs. When a
 872 particle hits a RPC, it induce a signal in the pickup strips of the RPC readout. If this
 873 signal is higher than the detection threshold, a LVDS signal is sent to the TDCs.
 874 The data is then organised into 4 branches keeping track of the event number, the
 875 hit multiplicity for the whole setup, and the time and channel profile of the hits in
 876 the TDCs.

877 5.3.2 RPC current, environmental and operation parameter mon- 878 itoring

879 In order to take into account the variation of pressure and temperature between
 880 different data taking periods the applied voltage is corrected following the rela-
 881 tionship :

$$882 HV_{eff} = HV_{app} \times \left(0.2 + 0.8 \cdot \frac{P_0}{P} \times \frac{T}{T_0} \right) \quad (5.10)$$

882 where T_0 (=293 K) and P_0 (=990 mbar) are the reference values.

883 5.3.3 Measurement procedure

- 884 Insert a short description of the online tools (DAQ, DCS, DQM).
- 885 Insert a short description of the offline tools : tracking and efficiency algorithm.
- 886 Identify long term aging effects we are monitoring the rates per strip.

887 5.3.4 Longevity studies results

6

888

889

Investigation on high rate RPCs

890 **6.1 Rate limitations and ageing of RPCs**

891 **6.1.1 Low resistivity electrodes**

892 **6.1.2 Low noise front-end electronics**

893 **6.2 Construction of prototypes**

894 **6.3 Results and discussions**

7

895

896

Conclusions and outlooks

897 **7.1 Conclusions**

898 **7.2 Outlooks**

References

899

- 900 [1] CERN. Geneva. LHC Experiments Committee. *The CMS muon project :
901 Technical Design Report*. Tech. rep. CERN-LHCC-97-032. CMS Collabora-
902 ration, 1997.
- 903 [2] CERN. Geneva. LHC Experiments Committee. *Technical Proposal for the
904 Phase-II Upgrade of the CMS Detector*. Tech. rep. CERN-LHCC-2015-010.
905 CMS Collaboration, 2015.
- 906 [3] CERN. Geneva. LHC Experiments Committee. *CMS, the Compact Muon
907 Solenoid : technical proposal*. Tech. rep. CERN-LHCC-94-38. CMS Col-
908 laboration, 1994.
- 909 [4] M. Abbrescia et al. “Study of long-term performance of CMS RPC under
910 irradiation at the CERN GIF”. In: *NIMA* 533 (2004), pp. 102–106.
- 911 [5] H.C. Kim et al. “Quantitative aging study with intense irradiation tests for
912 the CMS forward RPCs”. In: *NIMA* 602 (2009), pp. 771–774.
- 913 [6] S. Agosteo et al. “A facility for the test of large-area muon chambers at high
914 rates”. In: *NIMA* 452 (2000), pp. 94–104.
- 915 [7] PoS, ed. *CERN GIF ++ : A new irradiation facility to test large-area par-
916 ticle detectors for the high-luminosity LHC program*. Vol. TIPP2014. 2014,
917 pp. 102–109.
- 918 [8] M. Abbrescia et al. “Cosmic ray tests of double-gap resistive plate chambers
919 for the CMS experiment”. In: *NIMA* 550 (2005), pp. 116–126.
- 920 [9] A. Fagot. *GIF++ DAQ v4.0*. 2017. URL: https://github.com/afagot/GIF_DAQ.
- 922 [10] CAEN. *Mod. V1190-VX1190 A/B, 128/64 Ch Multihit TDC*. 14th ed. 2016.
- 923 [11] CAEN. *Mod. V1718 VME USB Bridge*. 9th ed. 2009.
- 924 [12] W-Ie-Ne-R. *VME 6021-23 VXI*. 5th ed. 2016.
- 925 [13] Wikipedia. *INI file*. 2017. URL: https://github.com/afagot/GIF_DAQ.
- 926

A

927

928 A data acquisition software for CAEN 929 VME TDCs

930 Certifying detectors in the perspective of HL-LHC required to develop tools for the
931 GIF++ experiment. Among them was the C++ Data Acquisition (DAQ) software
932 that allows to make the communications in between the computer and the TDC
933 modules in order to retrieve the RPC data [9]. In this appendix, details about the
934 software, as of how the software was written, how it functions and how it can be
935 exported to another similar setup.

936 **A.1 GIF++ DAQ file tree**

937 GIF++ DAQ source code is fully available on github at https://github.com/afagot/GIF_DAQ. The software requires 3 non-optional dependencies:

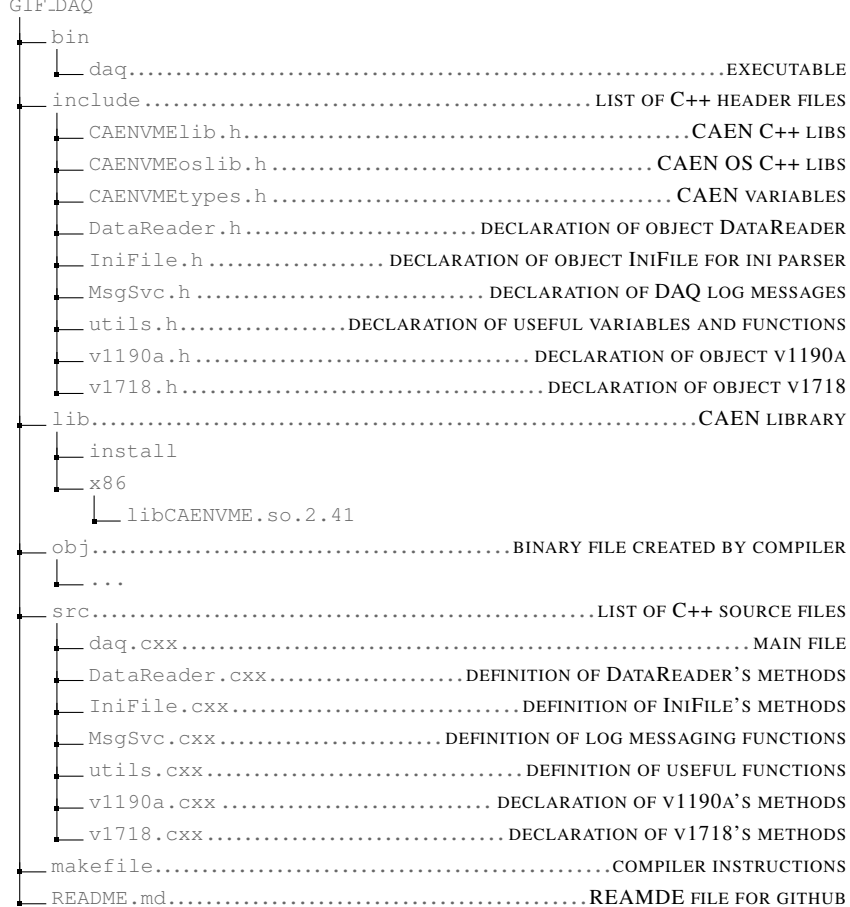
- 939 • CAEN USB Driver to mount the VME hardware
- 940 • CAEN VME Library to communicate with the VME hardware
- 941 • ROOT to organize the collected data into a TTree

942 The CAEN VME library will not be packaged by distributions and will need
943 to be installed manually. To compile the GIF++ DAQ project via a terminal, from
944 the DAQ folder use the command :

945 `make`

946 The source code tree is provided below along with comments to give an overview
 947 of the files' content. The different objects created for this project (v1718, v1190a,
 948 IniFile & DataReader) will be described in details in the following sections.

949



950 A.2 Description of the readout setup

951 The CMS RPC setup at GIF++ counts 5 V1190A Time-to-Digital Converter (TDC)
 952 manufactured by CAEN [10]. V1190A are VME units accepting 128 independent
 953 Multi-Hit/Multi-Event TDC channels whose signals are treated by 4 100 ps high
 954 performance TDC chips developped by CERN / ECP-MIC Division. The com-
 955 munication between the computer and the TDCs to transfer data is done via a
 956 V1718 VME master module also manufactured by CAEN and operated from a
 957 USB port [11]. These VME modules are all hosted into a 6U VME 6021 pow-

958 ered crate manufactured by W-Ie-Ne-R than can accomodate up to 21 VME bus
959 cards [12]. These 3 components of the DAQ setup are shown in Figure A.1.

960

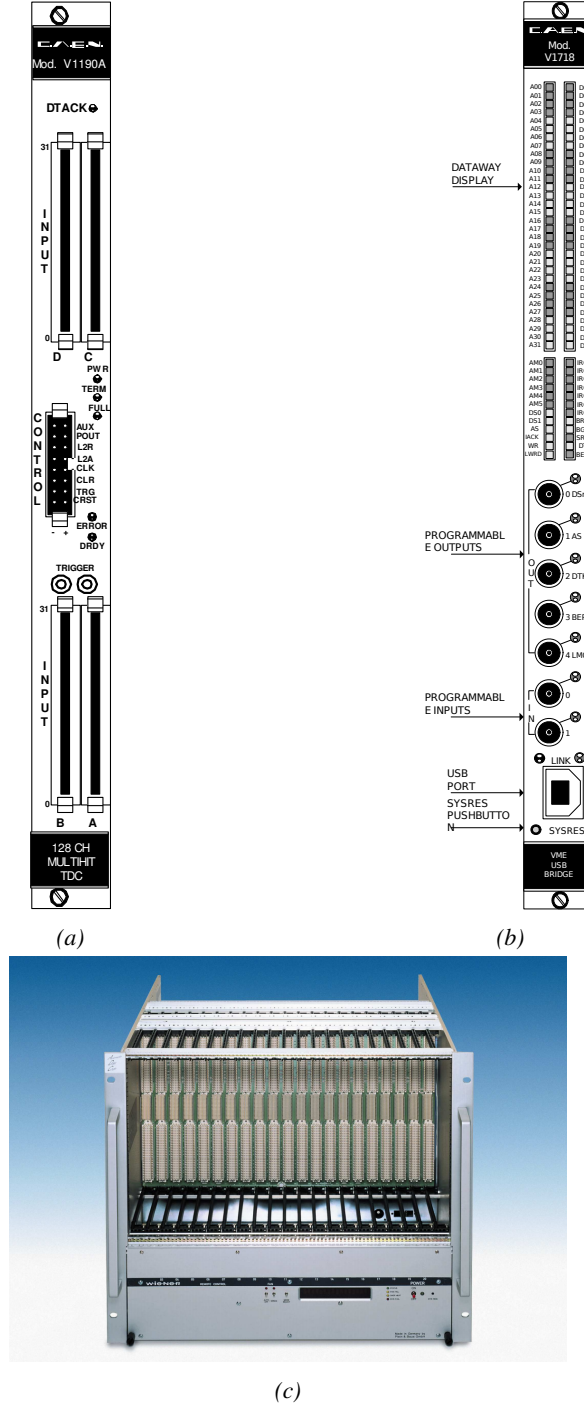


Figure A.1: (A.1a) View of the front panel of a V1190A TDC module [10]. (A.1b) View of the front panel of a V1718 Bridge module [11]. (A.1c) View of the front panel of a 6U 6021 VME crate [12].

961 A.3 Data read-out

962 To efficiently perform a data readout algorithm, C++ objects to handle the VME
 963 modules (TDCs and VME bridge) have been created along with objects to store
 964 data and read the configuration file that comes as an input of the DAQ software.
 965 It is useful to remind that the DAQ software in GIF++ is not a standalone software
 966 but is called through a Web Detector Control System (webDCS) application, that
 967 is the core of interactions with GIF++ setup, when data needs to be taken. Nev-
 968 ertheless, it is straight forward to make it into a standalone program that could be
 969 adapted to any VME setup using V1190A and V1718 modules.

970

971 A.3.1 V1190A TDCs

972 The DAQ used at GIF takes profit of the *Trigger Matching Mode* offered by V1190A
 973 modules. This setting is enabled through the method `v1190a::SetTrigMatching`
 974 (`int ntdcs`) where `ntdcs` is the total number of TDCs in the setup this setting
 975 needs to be enabled for (Source Code A.1). A trigger matching is performed in
 976 between a trigger time tag, a trigger signal sent into the TRIGGER input of the
 977 TDC visible on Figure A.1a, and the channel time measurements, signals recorded
 978 from the detectors under test in our case. Control over this data acquisition mode,
 979 explained through Figure A.2, is offered via 4 programmable parameters:

- 980 • **match window:** the matching between a trigger and a hit is done within a
 981 programmable time window. This is set via the method

```
982     void v1190a::SetTrigWindowWidth(Uint windowWidth, int ntdcs)
```

- 983 • **window offset:** temporal distance between the trigger tag and the start of
 984 the trigger matching window. This is set via the method

```
985     void v1190a::SetTrigWindowWidth(Uint windowWidth, int ntdcs)
```

- 986 • **extra search margin:** an extended time window is used to ensure that all
 987 matching hits are found. This is set via the method

```
988     void v1190a::SetTrigSearchMargin(Uint searchMargin, int ntdcs)
```

- 989 • **reject margin:** older hits are automatically rejected to prevent buffer over-
 990 flows and to speed up the search time. This is set via the method

```
991     void v1190a::SetTrigRejectionMargin(Uint rejectMargin, int ntdcs)
```

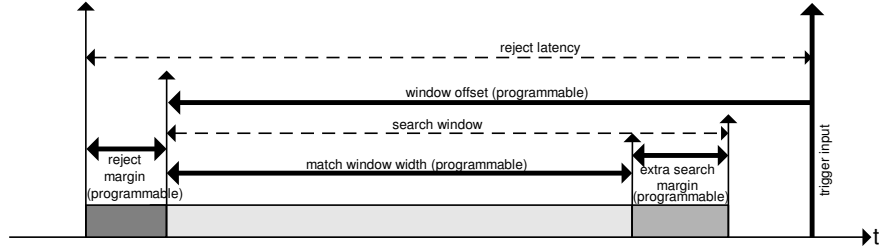


Figure A.2: Module V1190A Trigger Matching Mode timing diagram [10].

992 Each of these 4 parameters are given in number of clocks, 1 clock being 25 ns
 993 long. It is easy to understand at this level that there are 3 possible functioning
 994 settings:

- 995 • **1:** the match window is entirely contained after the trigger signal,
- 996 • **2:** the match window overlaps the trigger signal, or
- 997 • **3:** the match window is entirely contained before the trigger signal as dis-
 998 played on Figure A.2.

999 In both the first and second cases, the sum of the window width and of the
 1000 offset can be set to a maximum of 40 clocks, which corresponds to 1 μ s. Evidently,
 1001 the offset can be negative, allowing for a longer match window, with the constraint
 1002 of having the window ending at most 1 μ s after the trigger signal. In the third case,
 1003 the maximum negative offset allowed is of 2048 clocks (12 bit) corresponding to
 1004 51.2 μ s, the match window being strictly smaller than the offset. In the case of
 1005 GIF++, the choice has been made to use this last setting by delaying the trigger
 1006 signal. During the studies performed in GIF++, both the efficiency of the RPCs,
 1007 probed using a muon beam, and the noise or gamma background rate are moni-
 1008 tored. The extra search and reject margins are left unused.
 1009 To probe the efficiency of RPC detectors, the trigger time tag is provided by the
 1010 coincidence of scintillators when a bunch of muons passes through GIF++ area is
 1011 used to trigger the data acquisition. For this measurement, it is useful to reduce the
 1012 match window width only to contain the muon information. Indeed, the delay in
 1013 between a trigger signal and the detection of the corresponding muon in the RPC
 1014 being very constant (typically a few tens of ns due to jitter and cable length), the
 1015 muon signals are very localised in time. Thus, due to a delay of approximalety
 1016 325 ns in between the muons and the trigger, the settings where chosen to have a
 1017 window width of 24 clocks (600 ns) centered on the muon peak thanks to a nega-
 1018 tive offset of 29 clocks (725 ns).
 1019 On the otherhand, monitoring the rates don't require for the DAQ to look at a
 1020 specific time window. It is important to integrate enough time to have a robust

1021 measurement of the rate as the number of hits per time unit. The triggerring signal
 1022 is provided by a pulse generator at a frequency of 300 Hz to ensure that the
 1023 data taking occurs in a random way, with respect to beam physics, to probe only
 1024 the irradiation spectrum on the detectors. The match window is set to 400 clocks
 1025 (10 µs) and the negative offset to 401 clocks as it needs to exceed the value of the
 1026 match window.

1027

Source Code A.1: Description of C++ object v1190a.

```

1028 class v1190a
1029 {
  private :
    long             Handle;
    vector<Data32>   Address;
    CVDataWidth      DataWidth;
    CVAddressModifier AddressModifier;

  public:

    v1190a(long handle, IniFile *inifile, int ntdcs);
    ~v1190a();
    Data16 write_op_reg(Data32 address, int code, string error);
    Data16 read_op_reg(Data32 address, string error);
    void Reset(int ntdcs);
    void Clear(int ntdcs);
    void TestWR(Data16 value,int ntdcs);
    void CheckTDCStatus(int ntdcs);
    void CheckCommunication(int ntdcs);
    void SetTDCTestMode(Data16 mode,int ntdcs);
    void SetTrigMatching(int ntdcs);
    void SetTrigTimeSubtraction(Data16 mode,int ntdcs);
    void SetTrigWindowWidth(Uint windowHeight,int ntdcs);
    void SetTrigWindowOffset(Uint windowOffset,int ntdcs);
    void SetTrigSearchMargin(Uint searchMargin,int ntdcs);
    void SetTrigRejectionMargin(Uint rejectMargin,int ntdcs);
    void GetTrigConfiguration(int ntdcs);
    void SetTrigConfiguration(IniFile *inifile,int ntdcs);
    void SetTDCDetectionMode(Data16 mode,int ntdcs);
    void SetTDCResolution(Data16 lsb,int ntdcs);
    void SetTDCDeadTime(Data16 time,int ntdcs);
    void SetTDCHeadTrailer(Data16 mode,int ntdcs);
    void SetTDCEventSize(Data16 size,int ntdcs);
    void SwitchChannels(IniFile *inifile,int ntdcs);
    void SetIRQ(Data32 level, Data32 count,int ntdcs);
    void SetBlockTransferMode(Data16 mode,int ntdcs);
    void Set(IniFile *inifile,int ntdcs);
    void CheckStatus(CVErrorCodes status) const;
    int ReadBlockD32(Uint tdc, const Data16 address,
                     Data32 *data, const Uint words, bool ignore_berr);
    Uint  Read(RAWData *DataList,int ntdcs);
};


```

1030 The v1190a object, defined in the DAQ software as in Source Code A.1, offers
 1031 the possibility to concatenate all TDCs in the readout setup into a single object con-

1032 taining a list of hardware addresses (addresses to access the TDCs' buffer through
 1033 the VME crate) and each constructor and method acts on the list of TDCs.

1034

1035 A.3.2 DataReader

1036 Enabled thanks to `v1190a::SetBlockTransferMode(Data16 mode, int ntdcs)`,
 1037 the data transfer is done via Block Transfer (BLT). Using BLT allows to tranfer a
 1038 fixed number of events called a *block*. This is used together with an Almost Full
 1039 Level (AFL) of the TDCs' output buffers, defined through `v1190a::SetIRQ(Data32`
 1040 `level, Data32 count, int ntdcs)`. This AFL gives the maximum amount of
 1041 32735 words (16 bits, corresponding to the depth of a TDC output buffer) that
 1042 can wrten in a buffer before an Interrupt Request (IRQ) is generated and seen by
 1043 the VME Bridge, stopping the data acquisition to transfer the content of each TDC
 1044 buffers before resuming. For each trigger, 6 words or more are written into the
 1045 TDC buffer:

1046 • a **global header** providing information of the event number since the begin-
 1047 ning of the data acquisition,

1048 • a **TDC header**,

1049 • the **TDC data** (*if any*), 1 for each hit recorded during the event, providing
 1050 the channel and the time stamp associated to the hit,

1051 • a **TDC error** providing error flags,

1052 • a **TDC trailer**,

1053 • a **global trigger time tag** that provides the absolute trigger time relatively
 1054 to the last reset, and

1055 • a **global trailer** providing the total word count in the event.

1056 As previously described in Section 4.4.3, CMS RPC FEEs provide us with
 1057 100 ns long LVDS output signals that are injected into the TDCs' input. Any
 1058 avalanche signal that gives a signal above the FEEs threshold is thus recorded by
 1059 the TDCs as a hit within the match window. Each hit is assigned to a specific TDC
 1060 channel with a time stamp, with a precision of 100 ps. The reference time, $t_0 = 0$,
 1061 is provided by the beginning of the match window. Thus for each trigger, coming
 1062 from a scintillator coïncidence or the pulse generator, a list of hits is stored into
 1063 the TDCs' buffers and will then be transferred into a ROOT Tree.

1064

1065 When the BLT is used, it is easy to understand that the maximum number of
 1066 words that have been set as ALF will not be a finite number of events or, at least,

1067 the number of events that would be recorded into the TDC buffers will not be a
 1068 multiple of the block size. In the last BLT cycle to tranfer data, the number of
 1069 events to transfer will most propably be lower than the block size. In that case, the
 1070 TDC can add fillers at the end of the block but this option requires to send more
 1071 data to the computer and is thus a little slower. Another solution is to finish the
 1072 transfer after the last event by sending a bus error that states that the BLT reached
 1073 the last event in the pile. This method has been chosen in GIF++.

1074
 1075 Due to irradiation, an event in GIF++ can count up to 300 words per TDC. A
 1076 limit of 4096 words (12 bits) has been set to generate IRQ which represent from
 1077 14 to almost 700 events depending on the average of hits collected per event. Then
 1078 the block size has been set to 100 events with enabled bus errors. When an AFL
 1079 is reached for one of the TDCs, the VME bridge stops the acquisition by sending
 1080 a BUSY signal.

1081
 1082 The data is then transferred one TDC at a time into a structure called `RAWData`
 1083 (Source Code A.2).

1084

1085 *Source Code A.2: Description of data holding C++ structure `RAWData`.*

```
1086 struct RAWData{
 1087   vector<int>           *EventList;
 1088   vector<int>           *NHitsList;
 1089   vector<int>           *QFlagList;
 1090   vector<vector<int>>    *ChannelList;
 1091   vector<vector<float>>  *TimeStampList;
 1092 };
```

1087 In order to organize the data transfer and the data storage, an object called
 1088 `DataReader` was created (Source Code A.3). On one hand, it has `v1718` and `v1190a`
 1089 objects as private members for communication purposes, such as VME modules
 1090 settings via the configuration file `*iniFile` or data read-out through `v1190a::Read()`
 1091 and on the other hand, it contains the struture `RAWData` that allows to organise the
 1092 data in vectors reproducing the tree structre of a ROOT file.

1093

1094 *Source Code A.3: Description of C++ object `DataReader`.*

```

class DataReader
{
    private:
        bool      StopFlag;
        IniFile *iniFile;
        Data32   MaxTriggers;
        v1718    *VME;
        int       nTDCs;
        v1190a   *TDCs;
        RAWData  TDCData;

    public:
        DataReader();
        virtual ~DataReader();
        void     SetIniFile(string inifilename);
        void     SetMaxTriggers();
        Data32  GetMaxTriggers();
        void     SetVME();
        void     SetTDC();
        int      GetQFlag(Uint it);
        void     Init(string inifilename);
        void     FlushBuffer();
        void     Update();
        string  GetFileName();
        void     WriteRunRegistry(string filename);
        void     Run();
};

1095   Each event is transferred from TDCData and saved into branches of a ROOT
1096   TTree as 3 integers that represent the event ID (EventCount), the number of hits
1097   read from the TDCs (nHits), and the quality flag that provides information for any
1098   problem in the data transfer (qflag), and 2 lists of nHits elements containing the
1099   fired TDC channels (TDCh) and their respective time stamps (TDCTS), as presented
1100   in Source Code A.4. An example of ROOT data file is provided with Figure A.3.
1101
1102
1103   Source Code A.4: Highlight of the data transfer and organisation within
1104   DataReader::Run() after the data has been collected into TDCData.

```

```
RAWData TDCData;
TFile *outputFile = new TFile(outputFileName.c_str(), "recreate");
TTree *RAWDataTree = new TTree("RAWData", "RAWData");

int EventCount = -9;
int nHits = -8;
int qflag = -7;
vector<int> TDCCh;
vector<float> TDCTS;

RAWDataTree->Branch("EventNumber", &EventCount, "EventNumber/I");
RAWDataTree->Branch("number_of_hits", &nHits, "number_of_hits/I");
RAWDataTree->Branch("Quality_flag", &qflag, "Quality_flag/I");
RAWDataTree->Branch("TDC_channel", &TDCCh);
RAWDataTree->Branch("TDC_TimeStamp", &TDCTS);

for(UInt i=0; i<TDCData.EventList->size(); i++) {
    EventCount = TDCData.EventList->at(i);
    nHits = TDCData.NHitsList->at(i);
    qflag = TDCData.QFlagList->at(i);
    TDCCh = TDCData.ChannelList->at(i);
    TDCTS = TDCData.TimeStampList->at(i);
    RAWDataTree->Fill();
}

//...
//Here read the TDC data using v1190a::Read() and place it into
//TDCData for as long as you didn't collect the requested amount
//of data.
//...
```

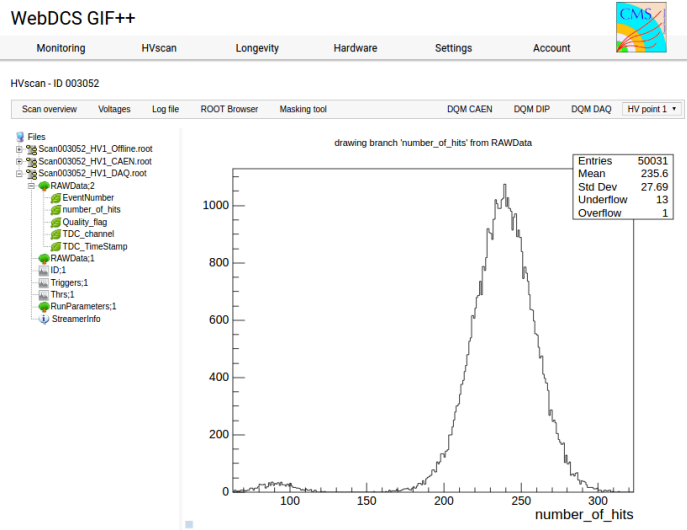


Figure A.3: Structure of the ROOT output file generated by the DAQ. The 5 branches (EventNumber, number_of_hits, Quality_flag, TDC_channel and TDC_TimeStamp) are visible on the left panel of the ROOT browser. On the right panel is visible the histogram corresponding to the variable nHits. In this specific example, there were approximately 50k events recorded to measure the gamma irradiation rate on the detectors. Each event is stored as a single entry in the TTree.

1105 A.3.3 V1718 USB Bridge

1106 In the previous section, the data transfer as been discussed. The importance of
 1107 the v1718 object (Source Code A.5), used as private member of DataReader,
 1108 was not explicited. VME master modules are used for communication purposes
 1109 as they host the USB port that connects the powered crate buffer to the com-
 1110 puter were the DAQ is installed. From the source code point of view, this ob-
 1111 ject is used to control the communication status, by reading the returned error
 1112 codes with v1718::CheckStatus(), or to check for IRQs coming from the TDCs
 1113 through v1718::CheckIRQ(). Finally, to ensure that triggers are blocked at the
 1114 hardware level, a NIM pulse is sent out of one of the 5 programmable outputs
 1115 (v1718::SendBUSY()) to the VETO of the coïncidence module where the trigger
 1116 signals originate from. As long as this signal is ON, no trigger can reach the TDCs
 1117 anymore.

1118

1119 *Source Code A.5: Description of C++ object v1718.*

```

class v1718{
    private:
        int Handle;
        Data32 Data;           // Data
        CVIRQLevels Level;     // Interrupt level
        CVAddressModifier AM;   // Addressing Mode
        CVDataWidth DataSize;   // Data Format
        Data32 BaseAddress;    // Base Address

    public:
        v1718(IniFile *inifile);
        ~v1718();
        long GetHandle(void) const;
        int SetData(Data16 data);
        Data16 GetData(void);
        int SetLevel(CVIRQLevels level);
        CVIRQLevels GetLevel(void);
        int SetAM(CVAddressModifier am);
        CVAddressModifier GetAM(void);
        int SetDatasize(CVDataWidth datasize);
        CVDataWidth GetDataSize(void);
        int SetBaseAddress(Data16 baseaddress);
        Data16 GetBaseAddress(void);
        void CheckStatus(CVErrorCodes status) const;
        void CheckIRQ();
        void SetPulsers();
        void SendBUSY(BusyLevel level);
};

1120

```

1121 A.3.4 Configuration file

1122 The DAQ software takes as input a configuration file written using INI standard [13].
 1123 This file is partly filled with the information provided by the shifters when starting
 1124 data acquisition using the webDCS, as shown by Figure A.4. This information is
 1125 written in section **[General]** and will later be stored in the ROOT file that con-
 1126 tains the DAQ data as can be seen from Figure A.3. Indeed, another `TTree` called
 1127 `RunParameters` as well as the 2 histograms `ID`, containing the scan number, start
 1128 and stop time stamps, and `Triggers`, containing the number of triggers requested
 1129 by the shifter, are available in the data files.

WebDCS GIF++

Monitoring HVscan Longevity Hardware Settings Account

DAQ High Voltage Scan

Type scan:	<input type="button" value="Rate Scan"/>	Comments:	<input type="text"/>
Source configuration:	<input type="button" value="Source OFF"/> <input type="button" value="U 333"/> <input type="button" value="D 333"/>	HV after scan:	<input type="button" value="Turn off"/>
Beam configuration:	<input type="button" value="Beam OFF"/>		
Waiting time:	<input type="text" value="1"/> (min)		
Trigger mode:	<input type="checkbox"/> External <input type="checkbox"/> Internal <input type="checkbox"/> Random		
Minimal measure time:	<input type="text" value="10"/> (min)		

Chamber	RE2-2-NPD-BARC-#	RE2-2-CERN-106	RE2-2-NPD-BARC-3	RE4-2-CERN-105	RE4-2-XCDBEL-1-4	Max triggers
HV _{eff} 1	8600	8500	8600	8500	6500	<input type="text"/>
HV _{eff} 2	8700	8600	8700	8600	6600	<input type="text"/>
HV _{eff} 3	8800	8700	8800	8700	6700	<input type="text"/>
HV _{eff} 4	8900	8800	8900	8800	6800	<input type="text"/>
HV _{eff} 5	9000	8900	9000	8900	6900	<input type="text"/>
HV _{eff} 6	9100	9000	9100	9000	7000	<input type="text"/>
HV _{eff} 7	9200	9100	9200	9100	7100	<input type="text"/>
HV _{eff} 8	9300	9200	9300	9200	7200	<input type="text"/>
HV _{eff} 9	9400	9300	9400	9300	7300	<input type="text"/>
HV _{eff} 10	9500	9400	9500	9400	7400	<input type="text"/>

Figure A.4: WebDCS DAQ scan page. On this page, shifters need to choose the type of scan (Rate, Efficiency or Noise Reference scan), the gamma source configuration at the moment of data taking, the beam configuration, and the trigger mode. These information will be stored in the DAQ ROOT output. Are also given the minimal measurement time and waiting time after ramping up of the detectors is over before starting the data acquisition. Then, the list of HV points to scan and the number of triggers for each run of the scan are given in the table underneath.

1130 The rest of the information is written beforehand in the configuration file tem-
 1131 plate, as explicited in Source Code A.6, and contains the hardware addresses to
 1132 the different VME modules in the setup as well as settings for the TDCs. As the
 1133 TDC settings available in the configuration file are not supposed to be modified, an
 1134 improvement would be to remove them from the configuration file and to hardcode
 1135 them inside of the DAQ code itself or to place them into a different INI file that
 1136 would host only the TDC settings to lower the probability for a bad manipulation
 1137 of the configuration file that can be modified from one of webDCS' menus.

1138

Source Code A.6: INI configuration file template for 4 TDCs. In section [General], the number of TDCs is explicated and information about the ongoing run is given. Then, there are sections for each and every VME modules. There buffer addresses are given and for the TDCs, the list of channels to enable is given. Finally, in section [TDCSettings], a part of the TDC settings are given.

```

1139 [General]
Tdc=4
ScanID=$scandid
HV=$HV
RunType=$runtype
MaxTriggers=$maxtriggers
Beam=$beam
[VMEInterface]
Type=V1718
BaseAddress=0xFF0000
Name=VmeInterface
[TDC0]
Type=V1190A
BaseAddress=0x00000000
Name=Tdc0
StatusA0-15=1
StatusA16-31=1
StatusB00-15=1
StatusB16-31=1
StatusC00-15=1
StatusC16-31=1
StatusD00-15=1
StatusD16-31=1
[TDC1]
Type=V1190A
BaseAddress=0x11110000
Name=Tdc1
StatusA00-15=1
StatusA16-31=1
StatusB00-15=1
StatusB16-31=1
StatusC00-15=1
StatusC16-31=1
StatusD00-15=1
StatusD16-31=1
1140 [TDC2]
Type=V1190A
BaseAddress=0x22220000
Name=Tdc2
StatusA0-15=1
StatusA16-31=1
StatusB00-15=1
StatusB16-31=1
StatusC00-15=1
StatusC16-31=1
StatusD00-15=1
StatusD16-31=1
[TDC3]
Type=V1190A
BaseAddress=0x44440000
Name=Tdc3
StatusA00-15=1
StatusA16-31=1
StatusB00-15=1
StatusB16-31=1
StatusC00-15=1
StatusC16-31=1
StatusD00-15=1
StatusD16-31=1
[TDCSettings]
TriggerExtraSearchMargin=0
TriggerRejectMargin=0
TriggerTimeSubtraction=0b1
TdcDetectionMode=0b01
TdcResolution=0b10
TdcDeadTime=0b00
TdcHead Trailer=0b1
TdcEventSize=0b1001
TdcTestMode=0b0
BLTMode=1

```

¹¹⁴¹ **A.3.5 DAQ algorithm overview**

¹¹⁴² **A.4 Software export**

B

1143

1144

Details on the online analysis package

1145

B.1 Introduction

1146

insert text here

C

1147

1148

1149

Structure of the hybrid simulation software

1150 C.1 Introduction

1151 insert text here...

